CrossMark

Inverse Calculation and Regularization Process for the Solar Aspect System (SAS) of HXI Payload on ASO-S Spacecraft

Ji-Rui Yu[1,2] , Ping Ruan[1], Yang Su[3,4], Ying-Hong He[1], Jin-You Tao[1], Zhe Zhang[3], Song Guo[1,2], Bin Xue[1], and Jian-Feng Yang[1]

[1] Xi'an Institute of Optics and Precision Mechanics of Chinese Academy of Sciences, Xi'an 710119, China; yujirui@opt.ac.cn
[2] University of Chinese Academy of Sciences, Beijing 100049, China
[3] Key Laboratory of Dark Matter and Space Astronomy, Purple Mountain Observatory, Chinese Academy of Sciences, Nanjing 210034, China
[4] School of Astronomy and Space Science, University of Science and Technology of China, Hefei 230026, China

Abstract

For the ASO-S/HXI payload, the accuracy of the flare reconstruction is reliant on important factors such as the alignment of the dual grating and the precise measurement of observation orientation. To guarantee optimal functionality of the instrument throughout its life cycle, the Solar Aspect System (SAS) is imperative to ensure that measurements are accurate and reliable. This is achieved by capturing the target motion and utilizing a physical model-based inversion algorithm. However, the SAS optical system's inversion model is a typical ill-posed inverse problem due to its optical parameters, which results in small target sampling errors triggering unacceptable shifts in the solution. To enhance inversion accuracy and make it more robust against observation errors, we suggest dividing the inversion operation into two stages based on the SAS spot motion model. First, the as-rigid-as-possible (ARAP) transformation algorithm calculates the relative rotations and an intermediate variable between the substrates. Second, we solve an inversion linear equation for the relative translation of the substrates, the offset of the optical axes, and the observation orientation. To address the ill-posed challenge, the Tikhonov method grounded on the discrepancy criterion and the maximum a posteriori (MAP) method founded on the Bayesian framework are utilized. The simulation results exhibit that the ARAP method achieves a solution with a rotational error of roughly $\pm 3''5$ (1/2-quantile); both regularization techniques are successful in enhancing the stability of the solution, the variance of error in the MAP method is even smaller—it achieves a translational error of approximately $\pm 18\ \mu$m (1/2-quantile) in comparison to the Tikhonov method's error of around $\pm 24\ \mu$m (1/2-quantile). Furthermore, the SAS practical application data indicates the method's usability in this study. Lastly, this paper discusses the intrinsic interconnections between the regularization methods.

Key words: methods: data analysis – Sun: flares – Sun: X-rays – gamma rays

1. Introduction

With the ongoing advancements in technology, there has been a renewed enthusiasm for solar investigation. In recent years, China's heliophysical research has advanced significantly, yielding numerous representative outcomes and executing some space-based solar expedition missions with specific objectives (Gan et al. 2019a). The ASO-S mission was born under this opportunity, it is China's inaugural synthesized solar observatory satellite focused on detecting magnetic fields, flares, and coronal mass ejections of the Sun (Gan et al. 2019b). HXI is one of the three primary loads designed specifically for detecting solar flares at hard X-ray spectra. Its imaging utilizes a space-modulated dual grating collimator instrument, as the principle of this imaging technique requires the exact relative positioning of the grating slits (Su et al. 2019) and the precise solar orientation simultaneously (Zhang et al. 2019), which can otherwise negatively impact the accuracy of the flare intensity distribution inversion. To ensure this, an online monitoring system, integrated with the instrument, is necessary to measure the collimator's status and observation direction. The Solar flare detection payloads that have been launched are all contained comparable systems. For instance, the Solar Aspect System (SAS) in RHESSI achieves a solar pointing accuracy of $0''4$ while the Twist Monitoring System yields a torsion measurement accuracy of a few arcsec (Zehnder et al. 2003). The STIX payload, launched in 2020 onboard the Solar Orbiter, also featured an SAS with a solar pointing accuracy of $\pm 4''$ (Krucker et al. 2020; Warmuth et al. 2020). In HXI, for the sake of measurement convenience, we choose the mature visual measurement scheme, which has been widely applied to different fields and scenarios, such as object detection (Zou et al. 2023), parameters measurement (Hashmi et al. 2022), structure and deformation monitoring (Dong & Catbas 2021; Zhuang et al. 2022), 3D reconstruction (Ham et al. 2019), robots (Abdulazeez & Faizi 2021), and Autonomous Vehicles (Joel et al. 2020). The SAS system uses the images to deduce

the deformation and observation orientation of the collimator by tracking the movement of a light spot. However, the significant differences in the parameters of the two lenses of SAS lead to a minute eigenvalue of the coefficient matrix in the inversion function. This is a common ill-posed inverse problem (Kabanikhin 2008; Engl & Groetsch 2014), where slight target sampling errors may result in oscillations and non-convergence of inversion results (Kabanikhin 2008; Engl & Groetsch 2014), making it impossible to meet the accuracy requirements with conventional solution methods like Gaussian, Newtonian, or Least Squares Optimization.

To address the aforementioned issue, two primary studies were conducted: first, utilizing the rigid body transformation model to mitigate solution instability caused by outliers; and second, implementing the regularization method to tackle the pathological inverse problem. To accomplish this objective, we commence with the physical model of SAS measurements and divide the solution process into two stages. Initially, we resolve the intermediate variables from a fraction of the light spots in the system. Subsequently, we solve the remaining variables together with other characteristic light spots. One advantage of using this approach is the utilization of the as-rigid-as-possible (ARAP) algorithm in the initial stage. This algorithm is a highly efficient 3D morphology editing tool that can ensure maximum maintenance of the local mesh shape characteristics and produce a solution closely resembling a rigid-body transformation (Sorkine & Alexa 2007). The equations resolved during the second step following decomposition undergo formal simplification. However, the unresolved ill-posed problem presents an obstacle, which curbs the precision of the conclusive resolution. To address this issue, regularization theory is employed, a prevalent approach for dealing with ill-posed problems (Poggio et al. 1987; Hansen 2010). This method involves appending a penalty term to minimize the residuals norm, limiting the solution's scope so that it is no longer an "exact solution" but a harmonization of the residuals and the solution's range. Although this solution is not the precise value when the equations are solved rigorously (assuming that the equations are linear and of full rank), this resolution is still more acceptable than the non-convergence of the solution resulting from the ill-posedness of the equations.

To verify the method's effectiveness, we make simulations for the algorithm mentioned above. The results indicate that it solved the ill-posed problem that we encountered to a large extent. Besides, the method is of significant practical value as it is implemented in the HXI instrument's actual production process. It helps in collimator assembly and grating adjustment and also achieves inflight monitoring and solar-pointing functions. Our research has assisted SAS in overcoming the limitations of its principle and improving its functionality, ensuring the success of the HXI observation mission. Furthermore, our findings highlight the optimization benefits of the regularization theory for ill-posed problems. This extends the potential application of visual measurement methods and provides valuable insights for the development of the next generation of solar observation equipment.

2. Measurement Principle

The SAS functions as a visual measurement system that solves the state of the HXI collimator through inverse analysis of light spot images. The system is comprised of two sub-optical systems, namely the deformation monitoring subsystem (DM) and the solar aspect subsystem (SA). The DM is a short-focus optical system that possesses a focal length of 32.8 mm, with a diagonal field of view (FOV) of $27°.8$. It captures images of both the three frosted glasses affixed to the front grating substrate and the Sun, producing four spots on the detector. The SA is a long-focus optical apparatus with a focal length of about 1214 mm and a diagonal FOV of $45'$, exclusively capable of imaging the Sun. Contrarily, the DM varies from the SA in that the DM lens is mounted on the SAS electronic control box, integrated with the detector, while the SA lens is suspended on the front substrate and positioned apart from the detector. The mounting configuration facilitates monitoring of the SA's optical lens by the DM as a feature point, thus constructing an additional equation to create a more complete physical model that represents a more realistic state of the collimator. Figure 1 displays the mounting state of SAS in HXI. Figure 2 explains how SAS works.

We identify four variables that need to be concerned when monitoring the collimator state, which: the relative rotation α of the front and rear grating substrates along the collimator main axis; the relative translation D perpendicular to the main axis between the front and rear grating substrates; the tilt offset β of the DM optical axis; and the tilt offset γ of the SA optical axis (also calibrated as the main axis of the collimator). We establish the motion pattern of the light spots to determine the four variables, of which α and d have a direct influence on the imaging effect on flares of the collimator and therefore are the main variables to be monitored by the SAS system. While β and γ are also the state variables of the HXI, but require less necessity for monitoring compared to α and D. It is mainly due to the fact that β represents the tilt of the SAS's optical axis, which does not influence the imaging effect, and the γ, while it affects the flare reconstruction by representing the Sun's pointing direction, its value can be attained through alternative methods, such as the direct measurement taken by the SA inflight.

To investigate the correlation between the motion patterns of light spots and the collimator state, we analyze three scenarios.

Case 1: The movement of the three frosted glass light spots is influenced by two factors: first, the relative rotation α and translation D that occur between the two grating substrates, and second, the axis offset β of the DM optical axis, which corresponds to the schematics shown in Figure 3(a).
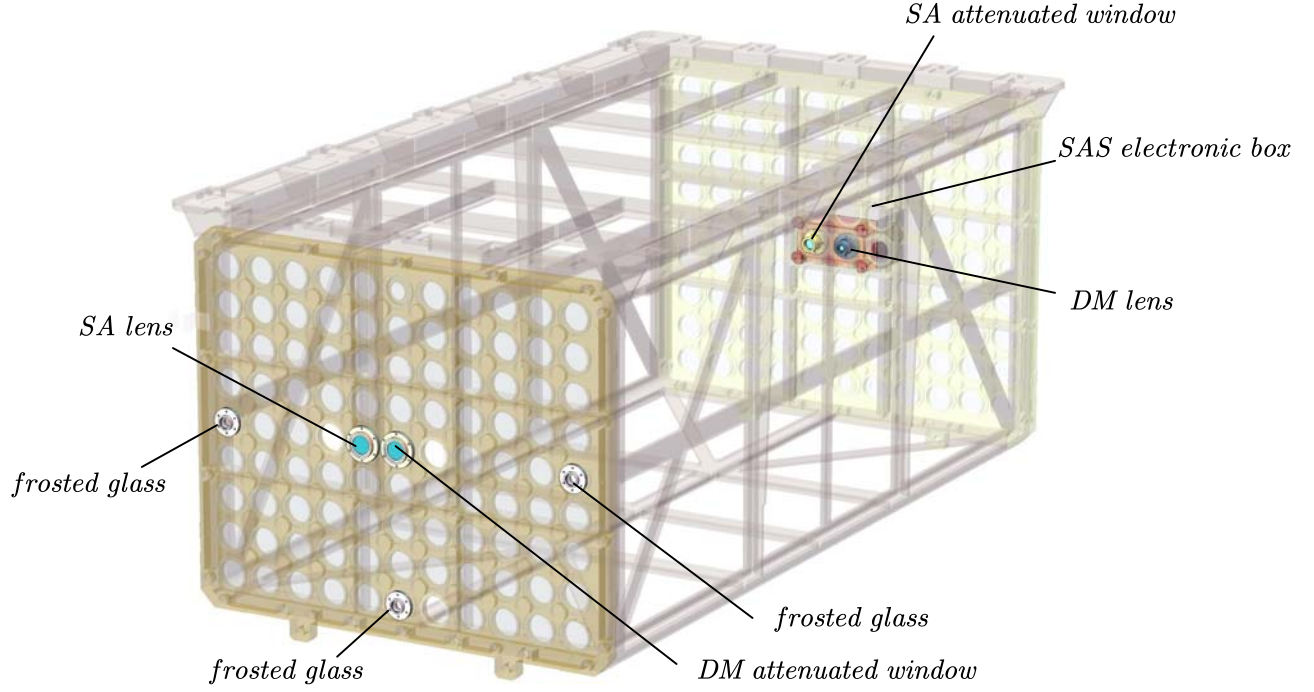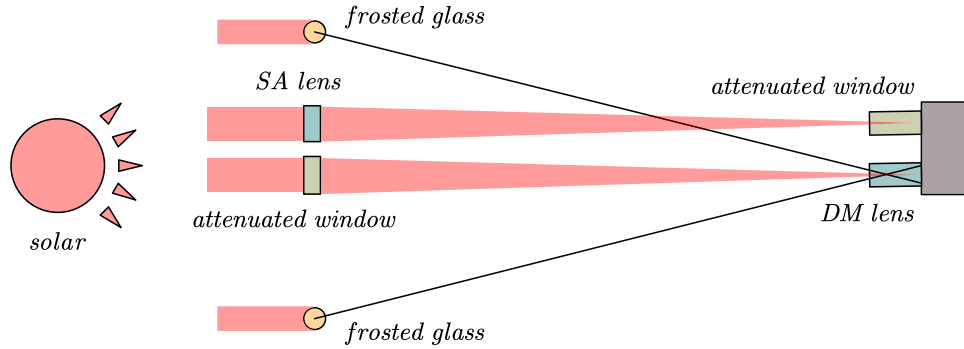
Figure 1. Layout of SAS in HXI.

Figure 2. The working principle of SAS.

Case 2: The motion of the DM solar light spot is due to two factors: the angular shift γ occurring in the SA optical axis (collimator main axis); or the offset β occurring in the DM optical axis, as shown in Figure 3(b).

Case 3: The movement of the SA solar light spot is influenced by two factors: the angular shift γ in the SA optical axis (collimator main axis) and the misalignment T in the SA optical lens concerning the detector, as shown in Figure 3(c).

To enhance our ability to create precise inversion equations, it is imperative that we calibrate the optical parameters of the DM and SA subsystems. Unlike the parameter calibration of a traditional vision measurement system, our focus is on the relationship between the motion mode of the target and its

corresponding light spots to satisfy the SAS function. It is proper to directly calibrate the intermediate parameters associated with the upper four variables in addition to the basic internal and external parameters, principal spot position, and aberration. The primary intermediate parameters are:

1. The proportionality K of the image point's movement resulting from the target's movement on the front substrate (such as hair glass or SA lens), as illustrated in Figure 4. Considering that the SAS system contains three frosted glasses, allowing for the utilization of the average of the three sets of quantities $K = (\sum_i^3 h_i / H_i)/3$.

2. The relationship between the angle shift of the DM optical axis and the corresponding movement of the light spot. For
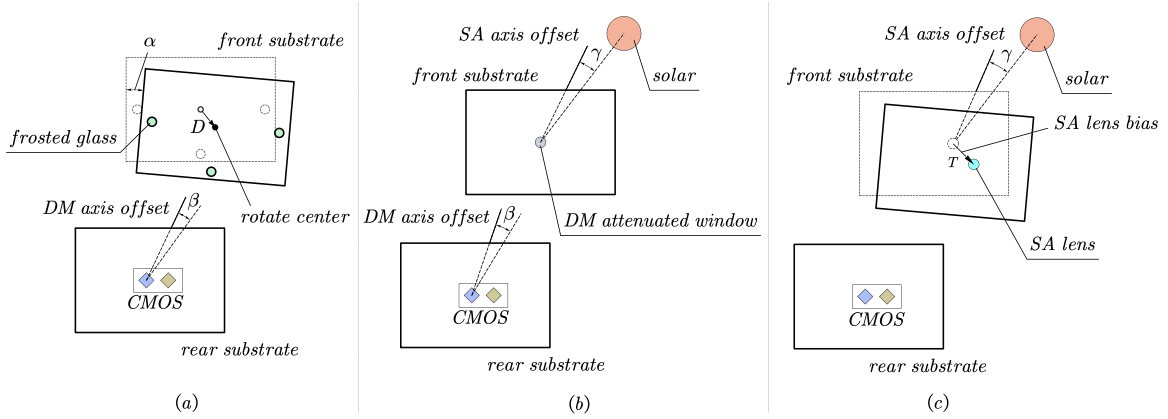
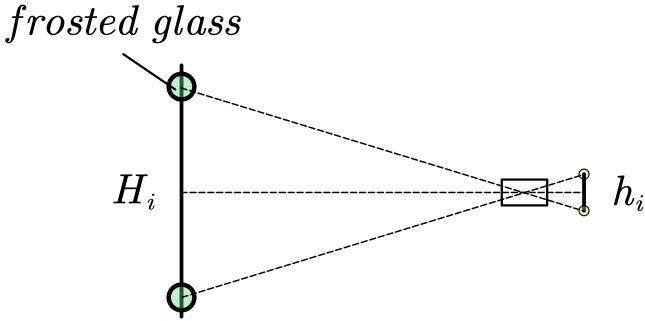**Figure 3.** Three types of light spots moving mode of SAS.

Figure 4. Parameter calibration with three frosted glasses.

the Sun target, it denotes by L_D, and has $L_D = x_D/\tan\theta_D$; For the frosted glasses target, it denotes by L_G and has $L_G = dl/d\theta_G = L_D \cdot \sec^2\theta_G$, as shown in Figure 5.

3. The relationship L_S between the angle shift of the SA optical axis and the corresponding movement of the light spot, which can be calculated by $L_S = x_S/\tan\theta_S$, as Figure 6 described.

The four intermediate parameters will constitute a crucial component in the development of SAS inversion equations. Further elaboration on these details will be provided in Section 3.3.

3. Data Processing and Regularization

Combining the physical model of the SAS, an inverse algorithm has been designed to compute the upper four variables. Due to the calculation complexity being beyond the capacity of the FPGA, the algorithm does not operate in flight. We just need to record the light spots' positions in orbit as input data and correspond it to some certain time point, such as the flare eruption, and then the inverse equation is solved on the ground subsequently. Thus, we obtain the instantaneous states

of the HXI collimator each time we are concerned. In the following context, the specific inverse equation set will be demonstrated and the ideology of how to resolve the equation will also be introduced.

In practice, the algorithm requires two types of input data: the position benchmark of the light spots' original location and their new position which occurs at a subsequent moment when changes may happen in the HXI system. Although five light spots can construct five formulas, only four unknown quantities need to be calculated, resulting in an overdetermined problem. Despite the possibility of solving it with a common numerical method, its ill-posed feature deems them all unfeasible. For this, the inverse process is divided into two subprocedures. The first involves computing the rotation and a so-called coupled displacement of the two substrates using the three frosted glass positions. The second involves determining the remaining variables using the outcomes from the first subprocedure and the positions of the solar light spot. Further explanation of these two subprocesses follows.

3.1. The Over-determined Function

The first subprocess that calculates the state between the two grid substrates is realized by the DM. Obviously, it is a common SLAM model that projects the object coordinate to the camera coordinate, the equation can be demonstrated as follows:

$$p' = \mathcal{K} \cdot p. \tag{1}$$

In the approximate case of neglecting the Z direction, $p = [x, y, 1]^T$ represents the reference position of the three frosted glasses, while $p' = [x', y', 1]^T$ represents the deformation occurrence, they are both the input data. The $\mathcal{K}$ demonstrate the DM
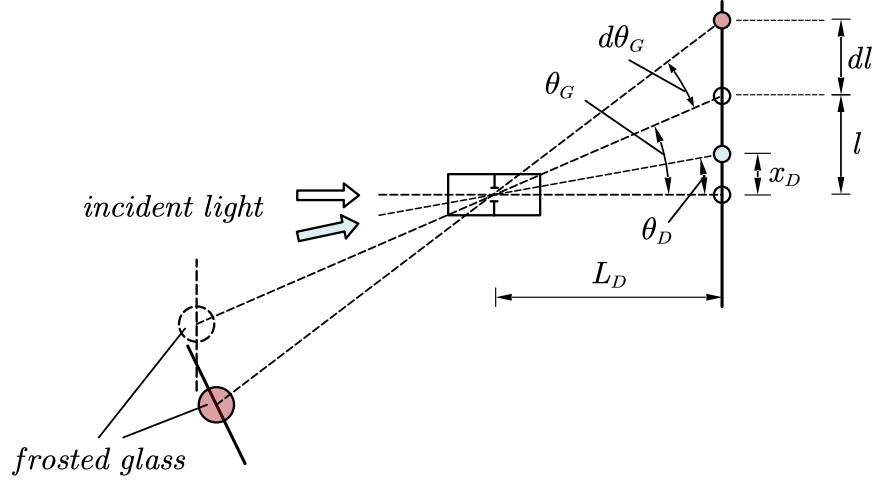
Figure 5. DM parameter calibration.

projection matrix with the form of:

$$\mathcal{K} = \begin{bmatrix} \cos\alpha & -\sin\alpha & c_x \\ \sin\alpha & \cos\alpha & c_y \\ 0 & 0 & 1 \end{bmatrix} \qquad (2)$$

where the quantity α represents the rotation of the two grid substrates, and $C = [c_x, c_y]^T$ is a so-called coupled displacement coming from D and β. Combine the three light spots, Equation (1) comprises six formulas with the unknown quantities α, c_x, and c_y, it constitutes an over-determined question. Compared to the full rank equation, the over-determined problem here cannot achieve the absolute accuracy solutions but still has the advantage of obtaining a moderate solution that adapts to the measurement errors, such as the least squares (LS).

However, if the LS method is used to solve for (1) to evaluate the relative motion between grating substrates, it is necessary to determine the center point of rotation and translation first, otherwise different definitions of the center position will yield different translations, even to the extent that at a particular center of rotation the translation is 0, which corresponds to the front grating substrate sweeping around that point by an angle.

The definition of the center of rotation on the front grating substrate is based on the theoretical center of the DM attenuator window. However, as this position cannot be measured directly, a substitute is used, namely the center of the line between the two frosted glasses, denoted as p_c in Figure 7. Consequently, the rotation of the front grating substrate corresponds to the angle of rotation of all points around p_c, and the translation corresponds to the amount of movement of the p_c point. Specifically, the objective function in (3) is directly used to solve the rotation based on the location of the
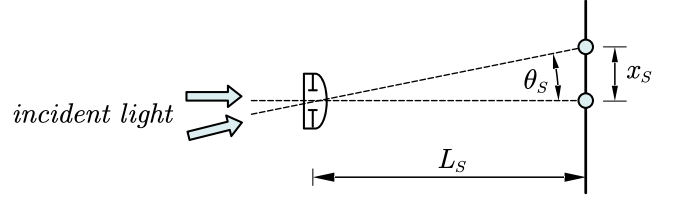

Figure 6. SA parameter calibration.

three frosted glasses, we have:

$$Q = \arg\min_{\alpha} \|p_i' - \mathcal{K}p_i\|_2^2, \quad i = 1, 2, 3 \qquad (3)$$

where p_i is the initial position of the three frosted glasses, and p_i' is the new position of the three frosted glasses. Then the coupled displacement is defined as:

$$C = p_c' - p_c \qquad (4)$$

where $p_c = (p_1 + p_2)/2$, and $p_c' = (p_1' + p_2')/2$.

3.2. The Rigid Transformation Model

In actual use, we discover the light spot position measurement errors that come from the center extract algorithm, or the instrument systemic errors, are a random quantity, which cannot be predicted and corrected. It introduces a non-existent deformation among the light spots' graph, which would mislead the LS solving process and cause an unexpected wrong value sometimes. The problem can be described as a non-rigid transform. To tackle the problem, we cite an ARAP iterative method that calculates the rigidity of the local transformations from the surface domain. The calculation results of this method can also be used as a comparative validation of the LS method. The ARAP separates
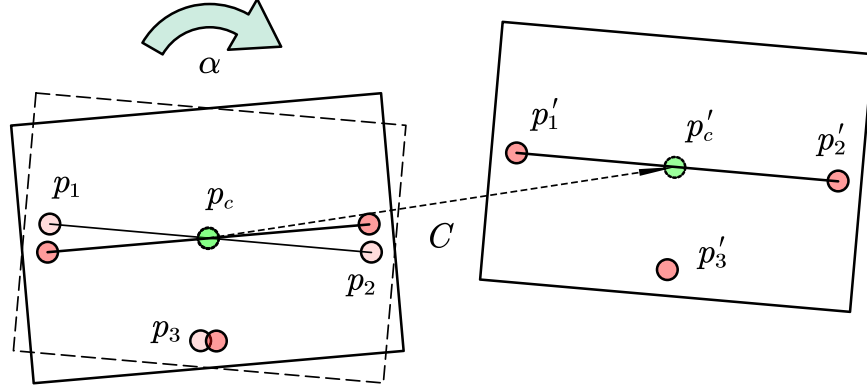
Figure 7. Patterns of rotation and translation of the front substrate. The rotation centern (green dot) is defined as the center of the connecting line of the frosted glasses 1 and 2.
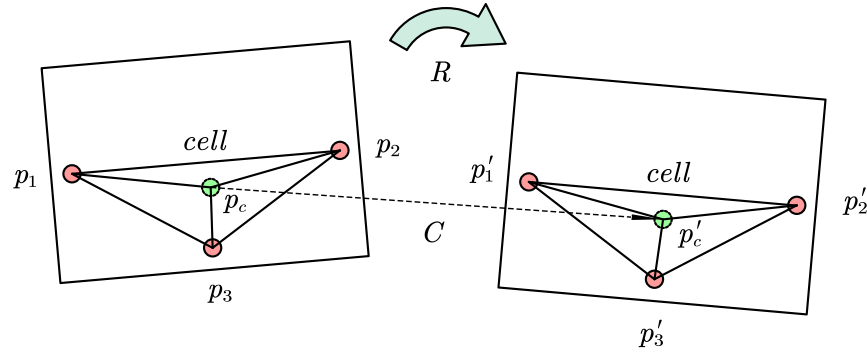

Figure 8. The cell structure on the front substrate. The red spots are the three frosted glasses, and the green spot is a virtual point that represent the rotation center.

the object graph into small cells, and combines the vertexes of each cell forming the "energy of cell," and the energy is demonstrated as Equation (5),

$$E(R_i, p_i') = \sum_{j \in N(i)} \omega_{ij} \|(p_i' - p_j') - R_i(p_i - p_j)\|^2 (i = 1 \cdots M)$$

$$(5)$$

where M is the sum of the points in the cell, $p_i = [x_i, y_i]^T$ is the known initial position of ith point, $p_i' = [x_i', y_i']^T$ is the new position after transformation, R_i denotes the rotation matrix that happened through the ith point in the model, $j \in N(i)$ represents the jth point that connecting to ith point, and $\| \cdot \|$ denotes the general norm. We can use Equation (5) to compute each cell point rotation $R = [R_i]$ and the coordinates $p' = [p_i']$ after the transform, the more minor the energy E, the higher rigidity of the cell shape. Constraining the cell energy minimum ensures that the transformation is computed with the cell shape as rigid as possible. It would eliminate the non-rigid effect to some extent and the solution accuracy and robustness would be increased considerably.

In the SAS, the frosted glasses form a triangle cell on the front grating substrate, as shown in Figure 8. The frosted glasses spots' positions p_i and p_i' are known input data, which means they could be regarded as constrain points. What is more, a virtual

"controlled point" that moves following the "constrain points" passively is desired to be defined as the rotation center, but also a translation center of the cell. Here we choose the geometry center of the frosted glasses p_1 and p_2 as the controlled point p_c as it simply corresponds to the real center of the front substrate. Finally, we obtain a cell with four points whose variations can explicitly characterize the deviation between the two grating substrates. The deviation can be divided into two parts, first is the rotation through the controlled point, and the other one is the displacement that corresponds to the movement of the controlled point.

Equation (5) is to compute two variables R and p_i' to minimize E, it is a nonlinear optimization problem that hard to find the global optimum. For simplicity, we utilize a Quasi-Newton method that fixes one variable value as known and calculates the other, then makes an exchange to realize the iteration to obtain the global optimization gradually. In practice, we first set an initial value for the controlled point and combine the observation data to form the p', then the cell vertex vectors can be defined as Equations (6) and (7):

$$e_{ij} = p_i - p_j \tag{6}$$

$$e_{ij}' = p_i' - p_j'. \tag{7}$$

By regarding the points' position values p' as known quantities, Equation (5) can change into matrix form:

$$E(R_i) = \sum_{i=1, j \in N(i)}^{M} \omega_{ij} \left(e'_{ij} - R_i e_{ij} \right)^T \left(e'_{ij} - R_i e_i j \right)$$

$$= \sum_{i=1, j \in N(i)}^{M} \omega_{ij} \left(e_{ij}'^T e'_{ij} - 2 e_{ij}'^T R_i e_{ij} + e_{ij}^T e_{ij} \right)^T. \quad (8)$$

$$A = \begin{bmatrix} \omega_{12} + \omega_{13} + \omega_{14} & -\omega_{12} & -\omega_{13} & -\omega_{14} \\ -\omega_{21} & \omega_{21} + \omega_{23} + \omega_{24} & -\omega_{23} & -\omega_{24} \\ -\omega_{31} & -\omega_{32} & \omega_{31} + \omega_{32} + \omega_{34} & -\omega_{34} \\ -\omega_{41} & -\omega_{42} & -\omega_{43} & \omega_{41} + \omega_{42} + \omega_{43} \end{bmatrix} \quad (14)$$

As Equation (8) is the function of variable R_i, the minimization of E only concerns the term R_i, which is

$$E(R_i) = \sum_{j \in N(i)} \left(-2 \omega_{ij} e_{ij}'^T R_i e_{ij} \right)$$

$$= \operatorname{argmaxTr} \left(R_i \sum_{j \in N(i)} \left(\omega_{ij} e_{ij} e_{ij}'^T \right) \right)$$

$$= \operatorname{argmaxTr}(R_i S_i). \quad (9)$$

The e_{ij} and e'_{ij} are column vectors that build a weighted square matrix S, where the

$$S_i = \sum_{j \in N(i)} \omega_{ij} e_{ij} e_{ij}'^T = U_i D_i V_i^T$$

and the matrix U_i, D_i, and V_i are derived from the singular value decomposition (SVD). In Equation (9), according to the rule of matrix trace, R_i would be chosen to satisfy the maximum of $\operatorname{Tr}(R_i S_i)$ when keeps the $R_i S_i$ a symmetric positive semi-definite matrix, thus, here the R_i value has:

$$R_i = V_i U_i^T. \quad (10)$$

It is the first iterative step we applied to obtain the rotation matrix R, and the second step is to use the known R value to deduce the new cell vertexes positions p'. At this time R is fixed, we get the p' by maximum the E value by the partial derivative calculation:

$$\frac{\partial E(R, p')}{\partial p'} = 0. \quad (11)$$

Equation (11) is a linear equation set contains M formula, which the ith formula has the form:

$$\sum_{j \in N(i)} \omega_{ij} (p'_i - p'_j) = \sum_{j \in N(i)} \frac{\omega_{ij}}{2} (R_i + R_j)(p_i - p_j). \quad (12)$$

While the unknown quantities p'_i in Equation (12) form a column vector, it can be transformed into a matrix form:

$$Ap' = b \quad (13)$$

where the coefficient matrix A elements are weighted by ω_{ij}:

and b is the right side of Equation (12). Actually, we only need to compute the controlled point position p'_c, as the constrained points position p'_k ($k \in$ constrain) is already determined by the input data. Thus the corresponding kth row and column of A, combining the kth row of b, are required to be removed, only leaving the elements concerning to the controlled point, then a new equation is reconstructed as:

$$A^r p'_c = b^r. \quad (15)$$

By solving Equation (15), the unknown controlled points p'_c are computed to satisfy the lowest energy of cells. In practice, we have three constrained points corresponding to the frosted glasses, as a result, Equation (15) has degenerated into a single element equation and the unique variable's solution p'_c demonstrates the new position of the rotation center.

Finally, the new rotation matrix R and new cell vertexes $p' = [p'_k, p'_c]$ are brought back into Equations (15) and (10) separately to perform the iteration process and stop at a suitable condition, such as when the amount of iterative change is less than a certain threshold. We use the rotation center to describe the rotation and translation of the substrate, thus, $R = R_c = \alpha$ and $C = p'_c - p_c$.

3.3. The Inverse Function

As previously stated, the ARAP algorithm provides solely a relative rotation α and coupled translation C between the front and rear substrates. To solve for the remaining state variables D, β, and γ, it is essential to establish the equations along with the motion pattern. Examining the first motion pattern in Figure 3(a), we can see that both D and β cause coupled translation C, enabling us to obtain the first equation of motion,

$$D + \beta \cdot L_G = C = p'_c - p_c. \quad (16)$$

Similarly, according to the second mode of motion Figure 3(b), the motion of the Sun light spot in the DM is jointly caused by β and γ, and the second equation of motion

can be obtained:

$$(\beta + \gamma) \cdot L_D = q' - q \qquad (17)$$

where q is the initial position of the DM Sun light spot and q' is the position after the instrument state change. According to the third motion model Figure 3(c), the motion of the SA Sun light spot is also synthesized by two factors, γ and T, respectively.

$$T + \gamma \cdot L_s = s' - s \qquad (18)$$

where s is the initial position of the SA solar light spot, and s' is the position of the spot after a state change occurred in the collimator. T is a special variable representing the offset produced by the lens in SA placed on the front substrate relative to the detector mounted on the rear substrate. Since the SA lens is also a target spot in the DM and is itself a quantity measured by the DM, T can be expressed in terms of the rotation and translation of the front substrate:

$$T = -\frac{t' - t}{B} \qquad (19)$$

where t is the initial coordinate of the SA lens captured through the DM, and t' is its new coordinate after translation and rotation followed by the front substrate, which has $t' = Rt + D$. The negative sign indicates the object-image opposite relationship. Note that the tangent calculations are simplified to arc angle calculation in Equations (16)–(18), taking into account that the actual deformation of the collimator is very small. Combine Equations (16)–(18), we determined the measurement equation set of the SAS:

$$By = g \qquad (20)$$

where

$$B = \begin{bmatrix} 1 & L_G & 0 \\ 0 & L_D & L_D \\ -1/K & 0 & L_S \end{bmatrix}$$

and its elements involve the optical parameters defined in Section 2. $y = [D\ \beta\ \gamma]^T$ is the vector to be solved. The right side vector

$$g = \begin{bmatrix} C \\ q' - q \\ s' - s + \dfrac{R \cdot t - t}{K} \end{bmatrix}$$

represents the observed data. So far, by back-calculating Equation (20),

$$y = B^{-1}g \qquad (21)$$

we realize the calculation of the state variables D, β, and γ.

3.3.1. Tikhonov Regularization Method

Equation (21) is a full-rank linear equation, commonly it can be straightly solved by Gaussian elimination or the Gaussian

Seidel method. Unfortunately, inspecting the condition number of matrix B described as $\text{cond}(B) = \|B^{-1}\|_2 \cdot \|B\|_2$, which illustrate the illness of a linear equation. A larger condition number represents a more unstable inverse solution to the equation and a more sensitive response to noise, such as, in Equation (20), we get an enormous condition number bigger than 440,000. To analyze the reasons, we research the solution structure with the SVD method, by matrix operation, the solution of the equation can be given by

$$y = B^{-1}g = \sum_i \frac{u_i^T g}{\sigma_i} v_i \qquad (22)$$

where u_i and v_i are the orthogonal column vectors of the SVD left and right matrix of B. σ_i is the singular value. It is obvious that the coefficients $u_i^T g/\sigma_i$ are impacted extremely by σ_i as it would decay into a tiny value in the ill-posed matrix. We impossibly get an ideal input g with no noise but a data $g + \Delta g$ with a perturbation, as a consequence, in the coefficient $u_i^T(g + \Delta g)/\sigma_i$, the perturbations Δg is magnified and causes the theoretical exact solution y becomes "unbounded." Thus, the traditional method cannot be used in the ill-posed problem computation, but some specialized approach is required. Equation (20) can be expressed as a least squares (LS) form:

$$Q = \min\{By - g\}. \qquad (23)$$

To restrict the range of possible solution values, a penalization term $\|y\|$ is introduced in Equation (23), which is known as regularization. Then Equation (23) becomes the following form:

$$Q = \arg\min_y \left\{ \|By - g\|_2^2 + \lambda^2\|y\|_2^2 \right\}. \qquad (24)$$

Consequently, the solution of Equation (24) can be reformulated as

$$y_\lambda = (B^TB + \lambda^2 I)^{-1}B^T g = \sum_i \varphi_i^{[\lambda]} \frac{u_i^T g}{\sigma_i} v_i \qquad (25)$$

where $\varphi_i^{[\lambda]} = \sigma_i^2/(\sigma_i^2 + \lambda^2)$. It adds a controlling weight that satisfies the demand, sometimes the method is called L-2 regularization or Tikhonov regularization. The λ is a positive parameter that balances the two parts, the residual norm $\|By - g\|_2$ and the solution norm $\|y\|_2$. The weight is enhanced to diminish the solution norm $\|y\|_2$ by enlarging the λ value, which can limit the uncontrollable perturbations in Equation (22) to some extent, but may cause a bigger deviation of between the regularization solution and the ideal solution due to the limitation of $\|By - g\|_2$ is expanded. On the contrary, if the λ is reduced, the regularization effect is weakened. The choice of λ value then becomes the core of the problem. There are many well-established methods for the selection of regularization parameters, such as the Discrepancy Principle (Engl 1987), the L-curve Criterion (Hansen 1992; Johnston & Gulrajani 2000), the Generalized Cross Validation

(Golub & von Matt 1997), and the Normalized Cumulative Periodogram (Mojabi & LoVetri 2008), etc. In this paper to compute the appropriate λ, we utilize the discrepancy principle, according to Equation (25), we can obtain:

$$
\begin{aligned}
By_\lambda - g &= USV^T \cdot \sum_i \frac{\sigma_i^2}{\sigma_i^2 + \lambda^2} \cdot \frac{u_i^T g}{\sigma_i} v_i - g \\
&= \sum_i \frac{\lambda^2}{\sigma_i^2 + \lambda^2} u_i u_i^T g.
\end{aligned}
\tag{26}
$$

Then the residual norm is:

$$
\|By_\lambda - g\|_2^2 = \sum_i \left(\frac{\lambda^2}{\sigma_i^2 + \lambda^2} \cdot u_i^T g \right)^2.
\tag{27}
$$

Taking into account the observation noise, there is $g = g^{\text{exact}} + e$. Based on the properties of SVD decomposition, the coefficient $u_i^T g^{\text{exact}}$ follows a monotonically decreasing pattern and satisfies the discrete Picard condition. There exists a bounding value t, when $\sigma_i < t$, because of the dominance of $u_i^T g^{\text{exact}}$, the $u_i^T g = u_i^T(g^{\text{exact}} + e)$ continues to decrease monotonically. However, the noise vector e may not align with g^{exact}, which means that $u_i^T e$ does not necessarily satisfy the discrete Picard condition. Consequently, when $\sigma_i > t$, the noise e is larger than g^{exact}, then the vector $u_i^T e$ will dominate leading to a platform or bounce in the value of $u_i^T g$ instead of decreasing, which would magnify the superimposed solution y_λ with tiny singular values. Hence, the main aim of the regularization process is to reduce this adverse effect, and the parameter $\varphi^{[\lambda]}$ works as the modifying factor. To analyze the effect of regularization parameters, we assume that the observation noise e is the Gaussian distributed with

$$
\text{Cov}(U^T e) = U^T E(e^T e) U = \eta^2 I,
$$

η is the standard deviation of e, then Equation (27) can be expressed as

$$
\begin{aligned}
\|By_\lambda - g\|_2^2 &= \sum_i \left[(1 - \varphi^{[\lambda]}) u_i^T g \right]^2 \\
&\approx \sum_{i=1}^{\lambda_\eta} \left[(1 - \varphi^{[\lambda]}) u_i^T g^{\text{exact}} \right]^2 + (n - \lambda_\eta)(1 - \varphi^{[\lambda]})^2 \|\eta\|_2^2
\end{aligned}
\tag{28}
$$

where λ_η is the boundary of the platform region and we have $E(\|e\|_2^2) = \|\eta\|_2^2$ that represents the expected value of the noise vector. As Equation (28) expression, the residual norm is composed of two parts, representing the effect of the observation error and the exact solution value on it, respectively. The $\|By_\lambda - g\|_2^2$ increases with the λ value increases, and e has a smaller value than g^{exact} commonly, whose proportion in the residual norm gradually diminishes along with the increasing of λ. Then we analyze two scenarios:

Case 1: there exists a critical value τ, when $\lambda < \tau$, the singular values slightly increase, and the divergence of the

superimposed solution $u_i^T g / \sigma_i$ remains dominated by noise e. This indicates under-regularization (under smoothing) and the solution $y \approx y^{\text{exact}}$.

Case 2: when $\lambda > \tau$, σ_i increases significantly, which largely suppresses the amplitude of the superimposed solution $u_i^T g / \sigma_i$. It demonstrates the over-regularization and the residual norm is collectively determined by both observation noise and exact observation value.

The discrepancy principle is to find a critical λ such that the residual norm is exactly dominated by the observation error e, i.e., there is $\|By_\lambda - g\|_2^2 = \|e\|_2^2$, which determines the regularization parameter that achieves equilibrium between the residual norm and the solution norm. This article advocates the use of the discrepancy principle when selecting the regularization parameter, owing to the ability to pre-evaluate the observation noise e (equivalent to the spot center extraction accuracy). Nevertheless, this still exists a potential risk, as an inadequate estimation of the observation error could significantly impact the solution outcomes, particularly when the parameter estimation is low, resulting in under-regularization that amplifies the range of the solution norm and causes the deviation of y^λ from the ideal solution y^* to be excessively large. To ensure caution, a safety factor ν around 2 is typically added to the noise for a slightly over-regularized state, then we have:

$$
\|By_\lambda - g\|_2 = \nu \|\eta\|_2.
\tag{29}
$$

According to Equation (29), we compute λ and substitute it into Equation (25) to obtain the regularized solution.

3.3.2. In Bayesian Perspective

Expanding on the Tikhonov regularization method discussed in Section 3.3.1, the Bayesian approach (Jin & Zou 2008a) offers fresh insight and makes a cross-validation of the solution of Equation (23). Assuming a prior distribution for the observation noise and the target variable, one can estimate unknown information by determining the posterior probability density function (PPDF). In the probabilistic perspective, the solution aims to determine the probability value that maximizes y, taking into account the known observation g, and uses the maximum a posteriori (MAP) of the y to estimate the optimal value. Based on the basic arithmetic of Bayesian estimation, there is

$$
\pi(y|g) = \frac{\pi(g|y)\pi(y)}{\pi(g)}
\tag{30}
$$

where $\pi(g|y)$ is the likelihood function, $\pi(y)$ is the prior probability of y (Jaynes 1968), and

$$
\pi(g) = \int \pi(g|y)\pi(y) dy
$$

is referred to as a normalized constant, which is usually ignored in calculations, then Equation (30) can be expressed as a

proportional relationship:

$$\pi(y|g) \propto \pi(g|y)\pi(y) \tag{31}$$

thus, MAP can estimate the y value:

$$y_{\mathrm{map}} = \arg\max \{\pi(y|g)\}. \tag{32}$$

To resolve the issue at hand, it is essential to acquire the probability prior and the probability likelihood as denoted in Equation (31). Initially, considering the noise of the observation, Equation (20) can be expressed as

$$g = By + e. \tag{33}$$

The observation noise e follows a continuous probability distribution at $\mathbb{R}^n$. Assuming the independence of e and y, the observation g is consistent with the noise distribution

$$\pi(g|y) = \pi(e) = \pi(g - By). \tag{34}$$

Usually, the noise e is the independent identically distributed Gaussian random variables with mean zero and standard deviation σ_1. Equation (34) is given by

$$\begin{aligned}\pi(g|y) &= \frac{1}{\sqrt{2\pi}\,\sigma_1}\exp\left(-\frac{e^2}{2\sigma_1^2}\right)\\ &= \frac{1}{\sqrt{2\pi}\,\sigma_1}\exp\left(-\frac{\|By - g\|^2}{2\sigma_1^2}\right).\end{aligned} \tag{35}$$

Defining the a priori probability $\pi(y)$ presents difficulty as the quantity of deformation y in SAS measurements is unknown. Consequently, we should assume the HXI instrument tends to stabilize, with minimal deformation in the absence of other interferences, and a lower likelihood of larger deformations. It thus follows a Gaussian distribution with parameter $(0, \sigma_2)$

$$\pi(y) = \frac{1}{\sqrt{2\pi}\,\sigma_2}\exp\left(-\frac{y^2}{2\sigma_2^2}\right). \tag{36}$$

Combining Equations (31), (35), and (36), we obtain

$$\pi(y|g) \propto \exp\left(-\frac{\|By - g\|^2}{2\sigma_1^2}\right)\exp\left(-\frac{\|y\|^2}{2\sigma_2^2}\right) \tag{37}$$

then the object function of MAP is

$$Q = \arg\max_y \pi(y|g) = \arg\max_y \exp\left(-\frac{\|By - g\|^2}{2\sigma_1^2} - \frac{\|y\|^2}{2\sigma_2^2}\right) \tag{38}$$

or another form

$$Q = \arg\min_y \left\{\frac{\|By - g\|^2}{2\sigma_1^2} + \frac{\|y\|^2}{2\sigma_2^2}\right\}. \tag{39}$$

Comparing Equations (24) and (39), it reveals that the regularization parameter resembles the probabilistic model parameter utilized in the Bayesian framework. We introduce a hyper-parameter λ in Equation (31), which is also a random

variable and helps to establish the correlation between the Bayesian model and the classical Tikhonov regularization theory. According to the Bayesian theorem, the PPDF is

$$\pi(y, \lambda|g) \propto \pi(g|y, \lambda) \cdot \pi(y|\lambda) \cdot \pi(\lambda). \tag{40}$$

As the observation g is not affected by the hyper-parameter λ, the first term on the right-hand side has $\pi(g|y, \lambda) = \pi(g|y)$. If the coefficient matrix $B \in \mathbb{R}^{m \times n}$, considering the interrelationships between observations, there exist

$$\pi(g|y) = \frac{1}{(2\pi)^{\frac{m}{2}}\sqrt{\det(S)}}\exp\left(-\frac{1}{2}(By - g)^T S^{-1}(By - g)\right). \tag{41}$$

In this article, g is composed of the computational center of three types of light spots, and the observation noise reflects the extraction accuracy of light spots. Since the components are independent, the noise has a covariance matrices as

$$S = \begin{bmatrix} \eta_c & & \\ & \eta_d & \\ & & \eta_s \end{bmatrix},$$

where η_c, η_d and η_s are the error variances of the three vectors of the observation data. Due to the regularization parameter being a penalty factor applied to the solution norm $\|y\|_2$, it is manifested as a correction of the prior probability $\pi(y|\lambda)$ within the Bayesian framework. As y follows a Gaussian distribution and its components satisfy the covariance matrix W (Calvetti & Somersalo 2018), for whom the λ serves as a scaling factor and ultimately modifying the solution norm of the y. In this scenario, y satisfies the Gaussian prior $\pi(y|\lambda) \sim N(0, \lambda W)$ with a hyper-parameters λ

$$\pi(y|\lambda) = \frac{1}{(2\pi)^{\frac{n}{2}} \cdot \sqrt{\det(\lambda W)}}\exp\left(-\frac{1}{2\lambda}y^T W^{-1}y\right) \tag{42}$$

considering that the components of y are independent of each other, then W must be a diagonal matrix. It is important to note that this paper analyses the different deformations represented by D, β, and γ according to the design specifications of the SAS, combined with certain empirical assumptions and simulation data. The argument is made that they should conform to different Gaussian priors. This involves estimating the variance of the deformation distributions based on the setup of the simulation inputs. It is stated that

$$W = \begin{bmatrix} \sigma_d^2 & & \\ & \sigma_\beta^2 & \\ & & \sigma_\gamma^2 \end{bmatrix},$$

where σ_d, σ_β, and σ_γ represent the standard deviation of the three preset deformations, respectively. $\pi(\lambda)$ represents the prior distribution of the hyper-parameters and can be described by the conjugate prior (Gelman et al. 1995). For this study, we
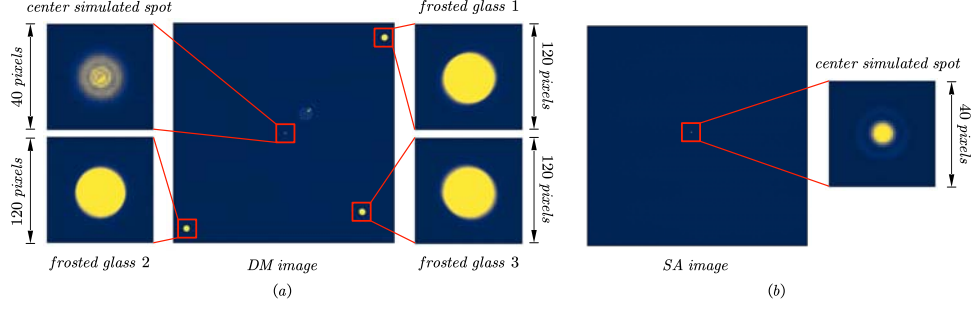
Figure 9. Different types of light spots in SAS in the ground test. Some simulated light sources are desired in the ground test. For frosted glasses, we used three LED light sources mounted only before the frosted glasses; a light pipe is the alternative to the incident solar light, and the quite tiny light spots are caused by its small FOV.

will use the gamma distribution with parameters α and β

$$\pi(\lambda) = \frac{\beta^\alpha}{\Gamma(\alpha)} \lambda^{\alpha-1} e^{-\beta\lambda} \quad (43)$$

where Γ is the gamma function. Bringing Equations (41), (42), and (43) into Equation (40), we obtain the joint PPDF of y and λ

$$\pi(y, \lambda|g) \propto \exp\left(-\frac{1}{2}(By - g)^T S^{-1}(By - g)\right)$$
$$\cdot \lambda^{-\frac{n}{2}} \exp\left(-\frac{y^T W^{-1} y}{2\lambda}\right) \cdot \lambda^{\alpha-1} \exp(-\beta\lambda) \quad (44)$$

then the objective function of MAP estimation can be easily determined

$$Q = \arg\min_{y,\lambda} \left\{ \frac{1}{2}\left((By - g)^T S^{-1}(By - g) + \frac{y^T W^{-1} y}{\lambda}\right) \right.$$
$$\left. + \left(\frac{n}{2} + 1 - \alpha\right) \ln(\lambda) + \beta\lambda \right\}. \quad (45)$$

The Equation (45) comprises two optimization variables, y and λ, which can be resolved via an iterative approach (Jiang et al. 2020).

Step 1: Define the initial value of the parameter λ_0, and subsequently, y_k for the kth iteration is evaluated in accordance with according to Equation (25)

$$y_k = \left(B^T S^{-1} B + \frac{W^{-1}}{\lambda_k}\right)^{-1} B^T S^{-1} g. \quad (46)$$

Step 2: Update the parameter λ_{k+1} by differential operation $\partial Q/\partial \lambda|_{y=y_k} = 0$, then λ_{k+1} satisfies the function

$$-\frac{y_k^T W^{-1} y_k}{2\lambda_{k+1}^2} + \frac{\frac{n}{2} + 1 - \alpha}{\lambda_{k+1}} + \beta = 0. \quad (47)$$

The iteration ends when the abort condition $\|y_n - y_{n-1}\| < \epsilon$ is met. We now achieve the estimated solution y with the Bayesian model, which is an approach that differs from the

Tikhonov regularization and denotes a cross-check of the certainty of the solution.

4. Numerical Simulation

For the procedures discussed previously, it is necessary to conduct simulations to assess their effectiveness in regularizing the ill-posed inverse problem in SAS. For this purpose, simulated data will be used to validate the accuracy of the inversion, and the results of real tests will be presented later. However, before this, we first calculate the light spot extraction accuracy of SAS, which serves as the observation error.

4.1. Accuracy of Light Spot Position

During both ground testing and inflight operations, SAS detects various types of light spots due to different illumination sources, as demonstrated in Figures 9 and 10. Different center coordinate extraction algorithms are implemented for the various forms of light spots, based on their distinguishing features.

1. Circular light spots with symmetric shape and uniform energy: binarized center of mass algorithm;
2. Bessel-shaped circular light spot: ellipse fitting center method (Fitzgibbon et al. 1999; Zhou et al. 2018);
3. Full-disk large circular light spot: four-quadrant area fitting algorithm or 14-row edge data fitting algorithm;

The principles behind these algorithms and the accuracy of the extraction will be thoroughly described in our forthcoming publication. Due to space constraints, we will be citing the findings and presenting the results in Table 1. It is evident that the extracting precision is equal to that of the noise level in the observed data g, which also serves as a crucial input for subsequent simulation calculations.

4.2. Operation Result

The numerical simulations conducted in this paper were executed on a computer equipped with an Intel Core i7 CPU and 16 GB of RAM, utilizing Python 3.8.5 to execute the
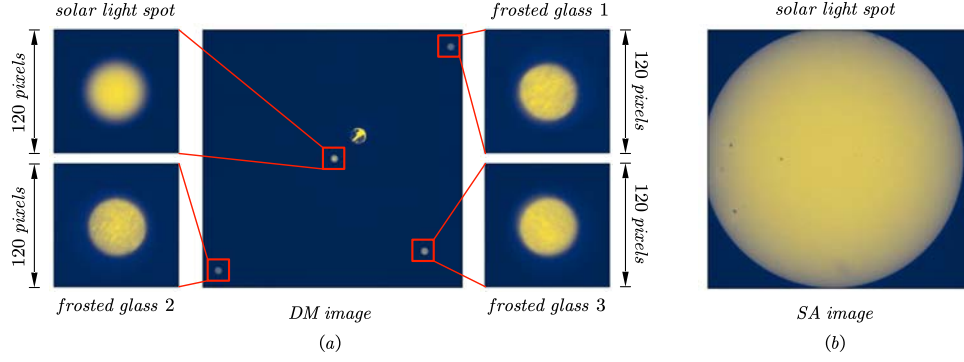
Figure 10. Different types of light spots in SAS inflight.

Table 1
Characteristics of Types of the Light Spots in SAS

Light Spot in SAS	Scenario	Morphological Structures	Extracting Method	Accuracy (Std)
Frosted glasses	Inflight use	Round spot	Shape centroid	0.04 pixels
	Ground test	Round spot	Shape centroid	0.04 pixels
Solar image in DM	Inflight use	Round spot	Shape centroid	0.04 pixels
	Ground test	Multi annulus	Ellipse fitting	0.025 pixels
Solar image in SA	Inflight use	Circle disk	Four quadrant method or 14-row fitting	0.11 pixels
	Ground test	Multi annulus	Shape centroid	0.04 pixels

algorithms. For all subsequent simulations, we established a consistent initial position g_0, for the spot and generated 1000 sets of deformations randomly to be implemented as simulations. The sequence employed for the simulations is as follows:

Step 1: Utilizing the imaging principle of SAS, we first derive the altered position g_1 of the light spot caused by simulated deformation. The resulting value $g = g_1 - g_0$, represents an ideal observation free from noise. It should be announced that the rotation and translation center of the front grating substrate is defined as the center of the line joining frosted glass 1 and 2 during the forward derivation of the changing coordinate g_1.

Step 2: To the ideal observation, we add an observed error $\bar{g} = g + e$, where e represents the extracting accuracy of the light spot center.

Step 3: Solving the rotation angle and coupled displacement with LS or ARAP method.

Step 4: Solving the inverse problem Equation (21) by utilizing the Tikhonov and Bayesian methods and subsequently evaluate the accuracy of the inversion algorithm.

It should be noted that we have made an assumption that any deformation in the HXI collimator during its full life cycle will not surpass the permissible threshold that would affect the quality of the flare imaging when conducting the numerical simulation. This constrains us to set the peak of simulated

deformation equal to the maximum allowable deformation of the collimator, whereby $\alpha = \pm 10''$ (the threshold that could impact imaging details), $d = \pm 18\,\mu$m (matching the period of the thinnest grating slit), $\beta = \pm 10''$, and $\gamma = \pm 10''$.

For comparison, it is assumed that there is no noise (i.e., $e = 0$), the results obtained from directly solving Equation (1) with the LS and ARAP methods, and Equation (21) using the Gaussian Elimination (GE) method, are presented in Figures 11 and 12. At this condition, the result demonstrates the high accuracy that reaches almost the zero inversion error. The LS method has higher inversion accuracy compared to the ARAP method, which is due to the fact that the ARAP does not solve the equations exactly, but instead calculates them through iterative optimization. These high accuracies show the correctness of the inverse process modeling.

Figures 13 and 14 display the outcomes upon adding the observation noise e into observation data g. The two methods, LS and ARAP, have very similar arithmetic results. The peak error of α is about $\pm 15''$, and the coupled displacement is about ± 0.1 pixels (as the C is an intermediate process variables, we demonstrate it in the "pixel" unit). Similarly, we analyze the error values at the 1/4, 1/2, and 3/4 quantile, which are indicated by each of the six black dashed lines in Figures 11–19. At the 1/2 quantile, the error of α is about $\pm 3''5$, and the error of c_x and c_y is about 0.03 pixels. In the
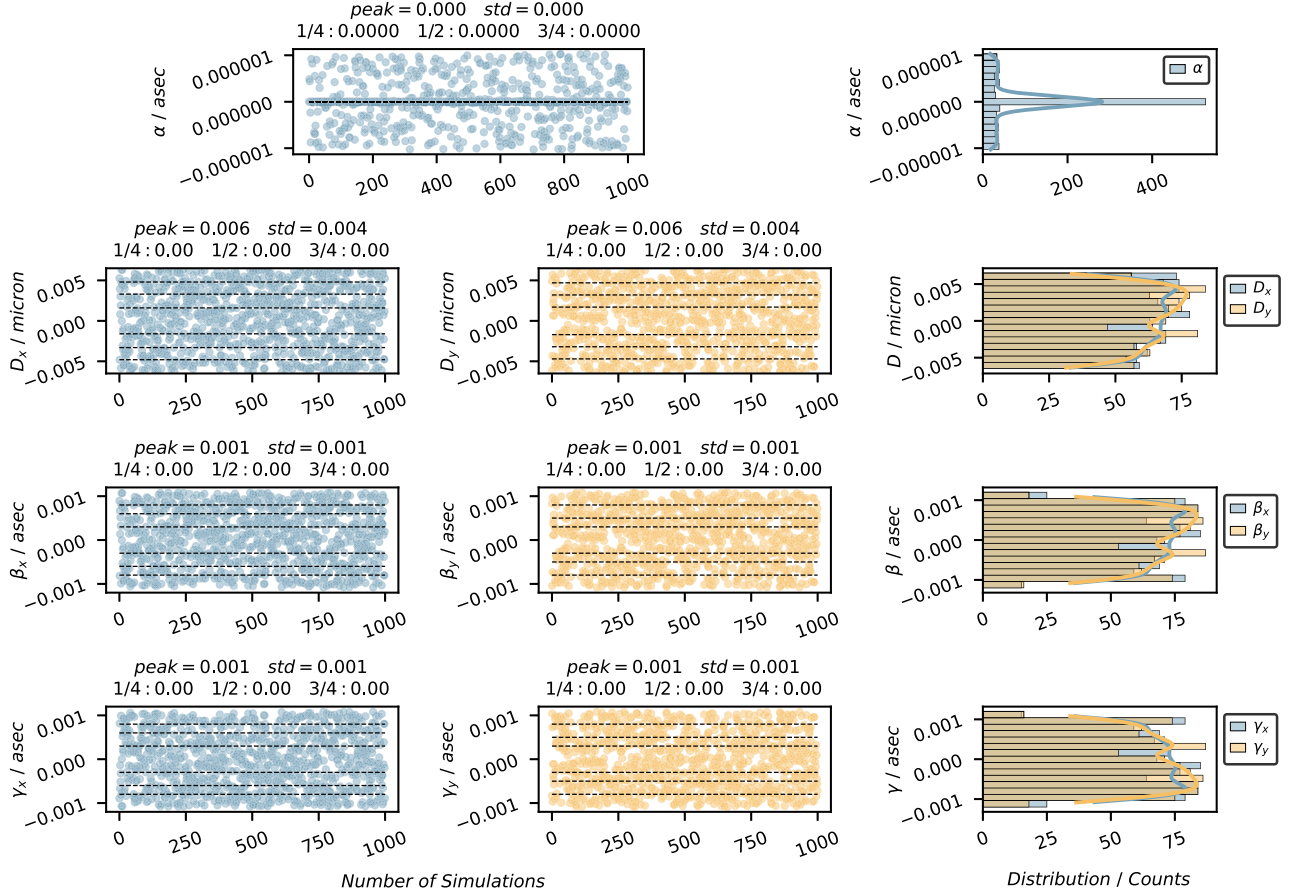
Figure 11. Inversion error distribution with the LS and GE methods without observed noise.

following numerical simulations, we use only the ARAP method to calculate the rotation angle for simplicity.

As a consequence, due to the ill-posed nature of the inverse function (21), an unregularized computation of the D, β, and γ variables, such as GE, results in a highly deviated and unacceptable solution that is far from ideal, as shown in Figure 15.

When using the Tikhonov method to solve Equation (21), the results are displayed in Figure 16. The α calculation is unaffected and retains the same accuracy of about $3''\!.5$, and regularization significantly optimizes the solution outcomes for D, β, and γ, whose peak error is approximately $\pm 55\,\mu$m, $\pm 10''$, and $\pm 10''$, respectively, and the errors displaying a uniform distribution within their peak range. At the $1/2$ quantile, the solution error is estimated to be around $D = \pm 24\,\mu$m, $\beta = \pm 5''$, and $\gamma = \pm 5''$.

The solution results utilizing the Bayesian framework exhibit distinct characteristics. The PPDF, which takes Gaussian noise and Gaussian prior distribution into account, generates an inverse error with a Gaussian distribution structure of a mean value of 0. This suggests that computation based on the

Bayesian framework is more likely to achieve smaller inversion errors, as illustrated in Figure 17. Based on the findings, the MAP produces slightly more significant peak errors than the Tikhonov approach. Specifically, the peak values for D is about $\pm 65\,\mu$m, β and γ are both slightly exceed $\pm 10''$. However, the error values at the $1/2$ quantile are lower, with $D = \pm 20\,\mu$m, $\beta = \pm 3''$, and $\gamma = \pm 3''$.

We have observed that the maximum error of the inversion changes with the preset simulated deformations. Specifically, when the preset deformations are large, the final inversion error increases, whereas it decreases when the deformations are small. Besides, the distributional characteristics of the error persist without alteration. For instance, the conclusions presented in Figures 16 and 17 are the outcomes acquired from a predetermined deformation of α within $\pm 10''$, D within $\pm 18\,\mu$m, β within $\pm 10''$, and γ within $\pm 10''$. By applying another set of predetermined values of α within $\pm 5''$, D within $\pm 5\,\mu$m, β within $\pm 3''$, and γ within $\pm 3''$, the inversion outcomes are exhibited in Figures 18 and 19. Compared to larger preset deformations, the computation of rotation does not present an ill-posed problem. Therefore, solution accuracy
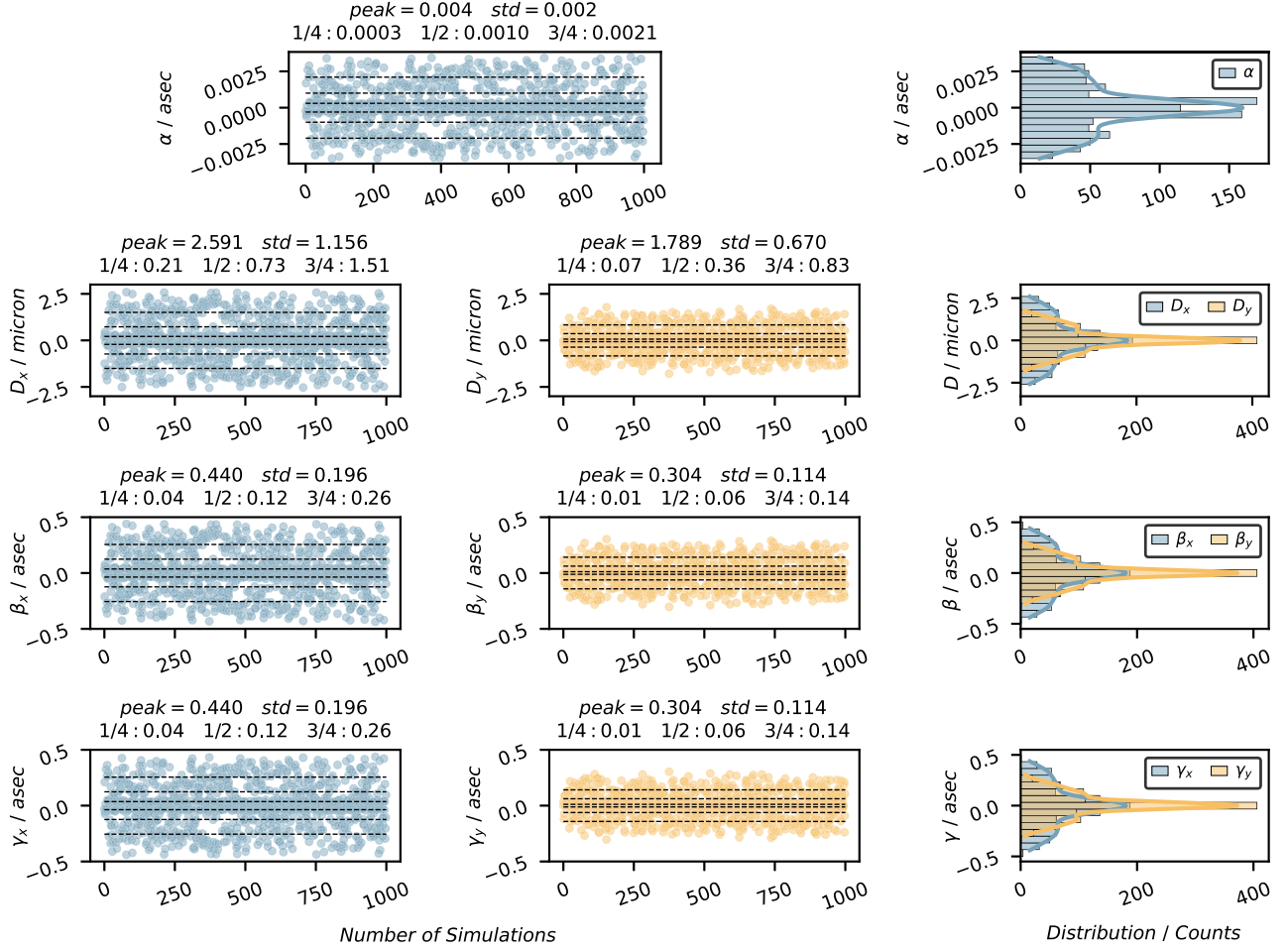
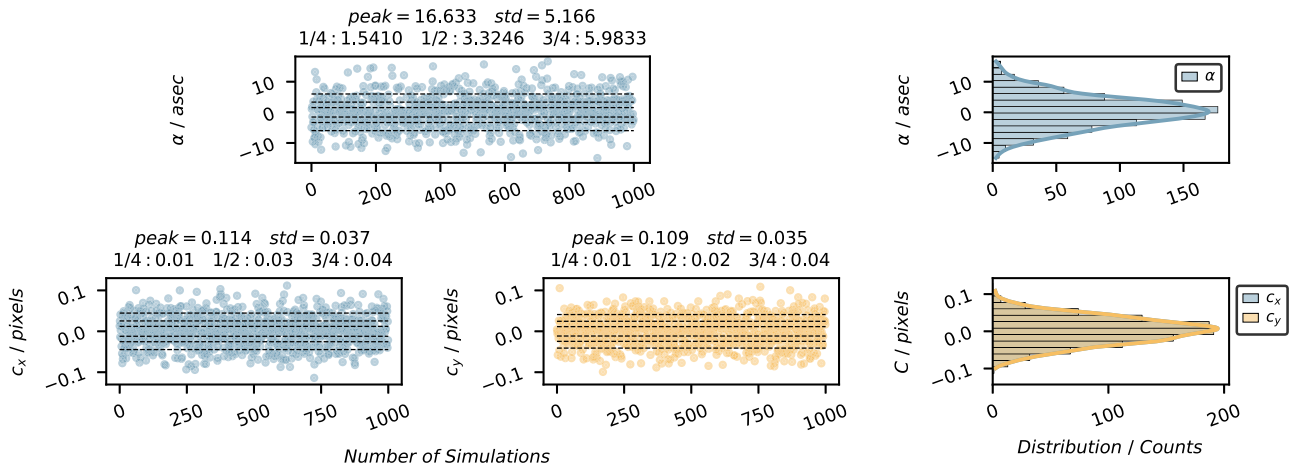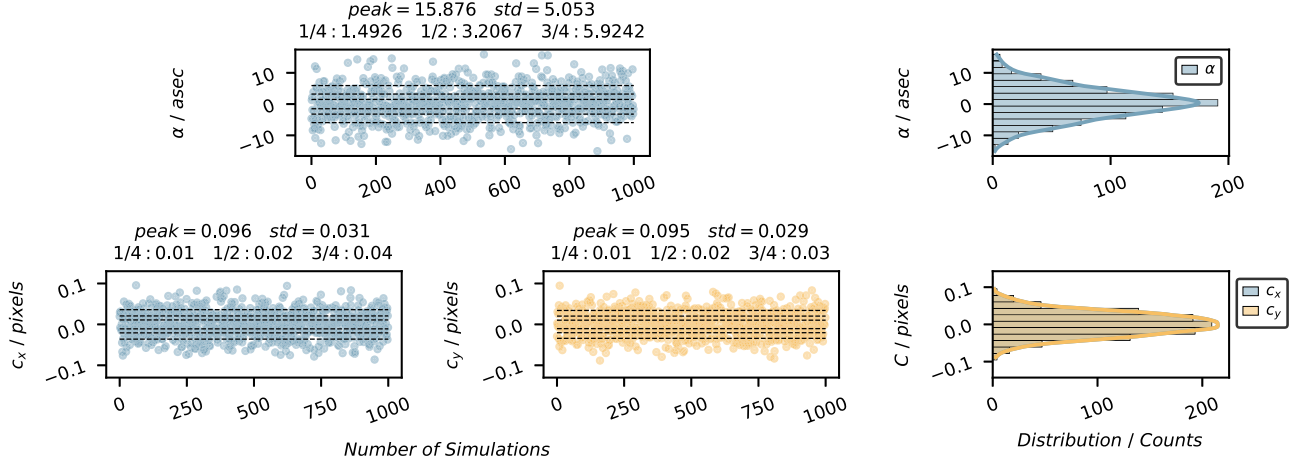**Figure 12.** Inversion error distribution with the ARAP and GE methods without observed noise.
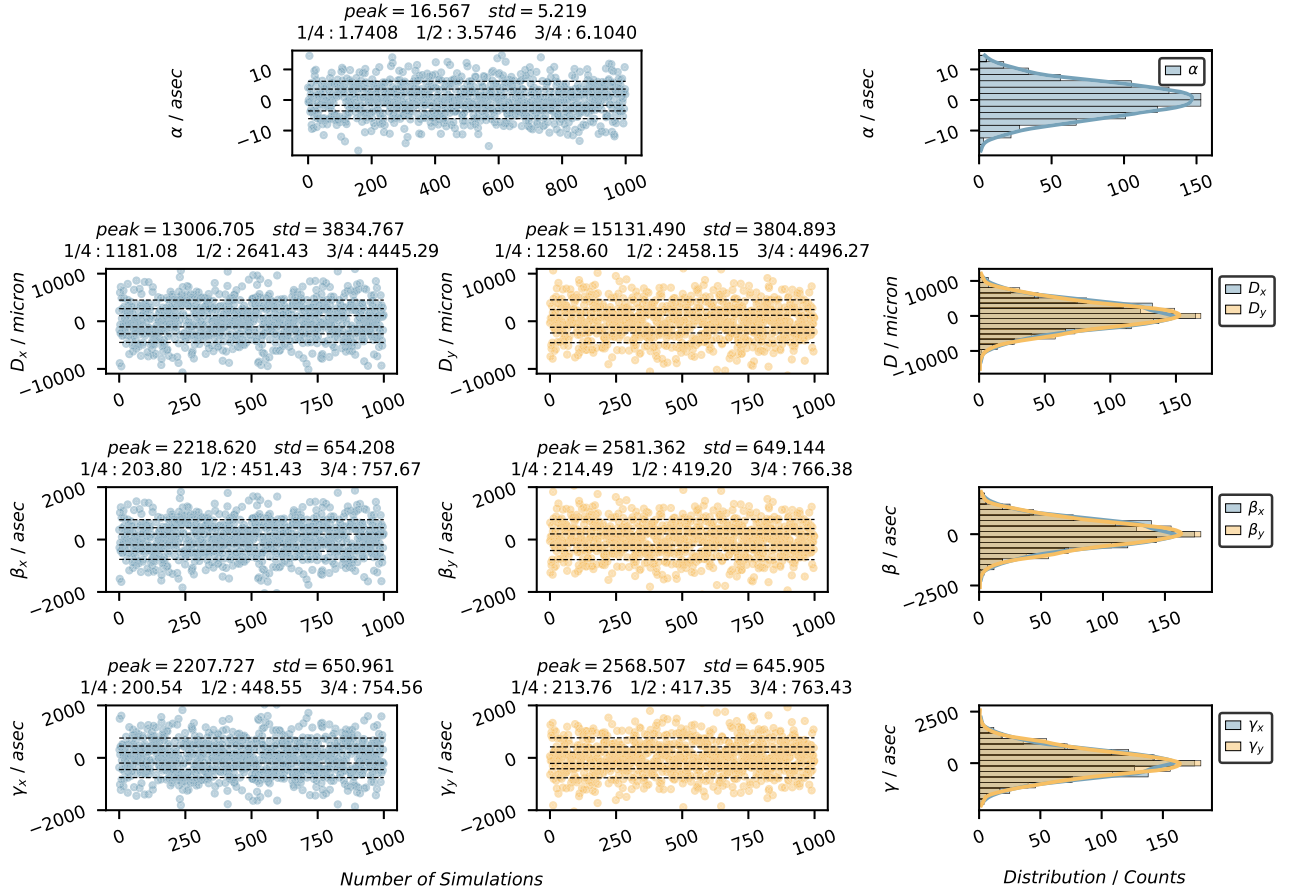

Figure 13. Rotation and coupled displacement error distribution using LS. The equation is solved with the Powell and BFGS methods, with the same result.

Figure 14. Rotation and coupled displacement error distribution using ARAP.

Figure 15. Direct inversion error distribution with the GE method adding observed noise.
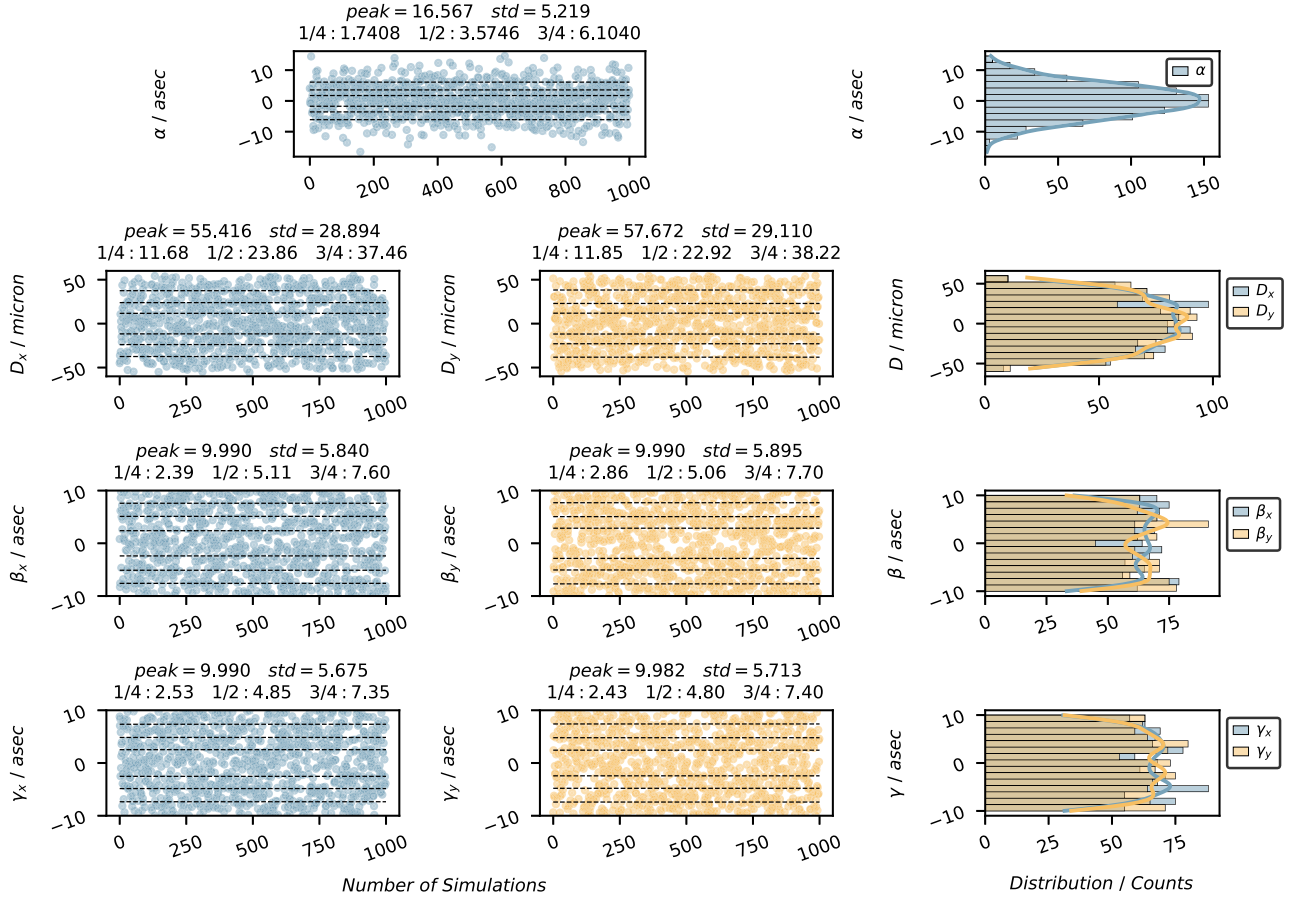
Figure 16. Inversion error distribution with the Tikhonov method.

remains unchanged. The peak error of D, β, and γ solutions is lower with the implementation of the Tikhonov method, which achieves a peak error of about $D = \pm 20\ \mu$m, $\beta = \pm 3''$, and $\gamma = \pm 3''$, and a 1/2-quantile error of $D = \pm 8\ \mu$m and $\beta = \pm 1''.5$, $\gamma = 1''.5$; The MAP method can achieve the highest error of about $D = \pm 25\ \mu$m, $\beta = \pm 4''$, $\gamma = \pm 4''$, and at the 1/2 quantile, the error values are $D = \pm 6\ \mu$m, $\beta = \pm 1''$, $\gamma = \pm 1''$. The error distributions of both methods are unaffected by the magnitude of the preset deformation. The reason is that, when carrying out regularization, the computation incurs a penalty factor in the form of the solution norm $\|y^*\|_2^2$, and for the identical inverse equation, the ideal solution norm increases as the preset deformation increases. At this time, to meet the optimization objective of Equation (24), the solution norm contour expands and intersects the smaller residual norm contour—resulting in a smaller $\|By - g\|_2^2$. Such regularization is inclined toward under-smoothing, leading to the inverse problem being closer to an unbiased solution. Hence, it achieves the "divergent" solution that has larger amplitude. In summary, a significant deviation in the collimator would

decrease the precision of the SAS monitoring, which necessitates the assumption that the instrument would not exhibit a substantial deviation, as indicated at the beginning. Furthermore, if the collimator indeed undergoes an unacceptably large deformation, which will compromise the imaging quality of the HXI instrument, it may not be necessary to prioritize the measurement accuracy of the SAS if the usability of the HXI cannot be ensured. Fortunately, the HXI underwent precise calibration using an X-ray beam, additionally, the installation and integration processes were in a relatively stable circumstance, and the instrument was accurately temperature-controlled inflight to ensure an unchanged state. Based on these factors, it is reasonable to assume that significant deformation would not occur in the collimator. These assumptions and conclusions were subsequently confirmed through inflight testing.

In summary, the simulation results are presented in a tabulated form for clarity. Table 2 compares the results obtained from inverting simulations using both Tikhonov regularization and Bayesian frameworks for large preset deformations. The MAP approach offers some advantages
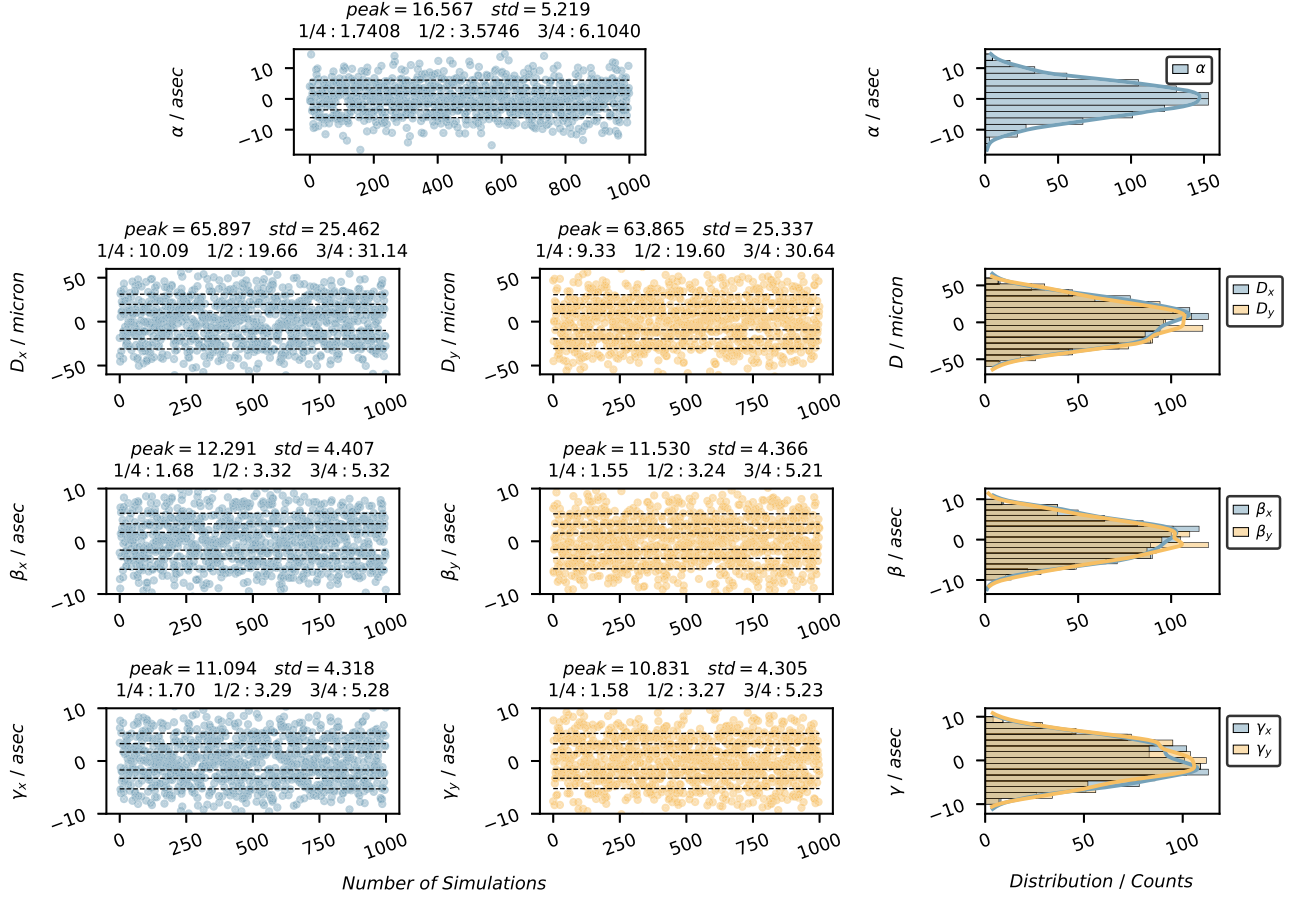
Figure 17. Inversion error distribution with the MAP method.

Table 2
Inversion Error with Large Preset Deformations

	Tikhonov					Bayesian				
	1/4 Quantile	1/2 Quantile	3/4 Quantile	Peak	Std	1/4 Quantile	1/2 Quantile	3/4 Quantile	Peak	Std
α(arcsec)	1.74	3.57	6.10	16.57	5.22	1.74	3.57	6.10	16.57	5.22
$d_x(\mu m)$	11.68	23.86	37.46	55.42	28.89	10.09	19.66	31.14	65.90	25.46
$d_y(\mu m)$	11.85	22.92	38.22	57.62	29.11	9.33	19.60	30.64	63.87	25.34
β_x(arcsec)	2.39	5.11	7.60	9.99	5.84	1.68	3.32	5.32	12.29	4.41
β_y(arcsec)	2.86	5.06	7.70	9.99	5.90	1.55	3.24	5.21	11.53	4.37
γ_x(arcsec)	2.53	4.85	7.35	9.99	5.68	1.70	3.29	5.28	11.09	4.32
γ_y(arcsec)	2.43	4.80	7.40	9.98	5.71	1.58	3.27	5.23	10.83	4.31

owing to the Gaussian distribution which guarantees a higher proportion of small errors, the results of these two methods will be jointly considered. Table 3 presents the inversion outcomes obtained with smaller preset simulated deformations, some corresponding values are smaller compared to Table 2. Since the simulation data utilizes 1000 groups of randomly preset values, each simulation could produce slightly varied outcomes, but the results remain at the same level. It is worth noting that the discrepancy principle is capable of reducing the peak error when it is over-regularized by increasing the safety factor ν. However, there is a potential risk of raising ν arbitrarily, due to the fact that it would constrain the inversion
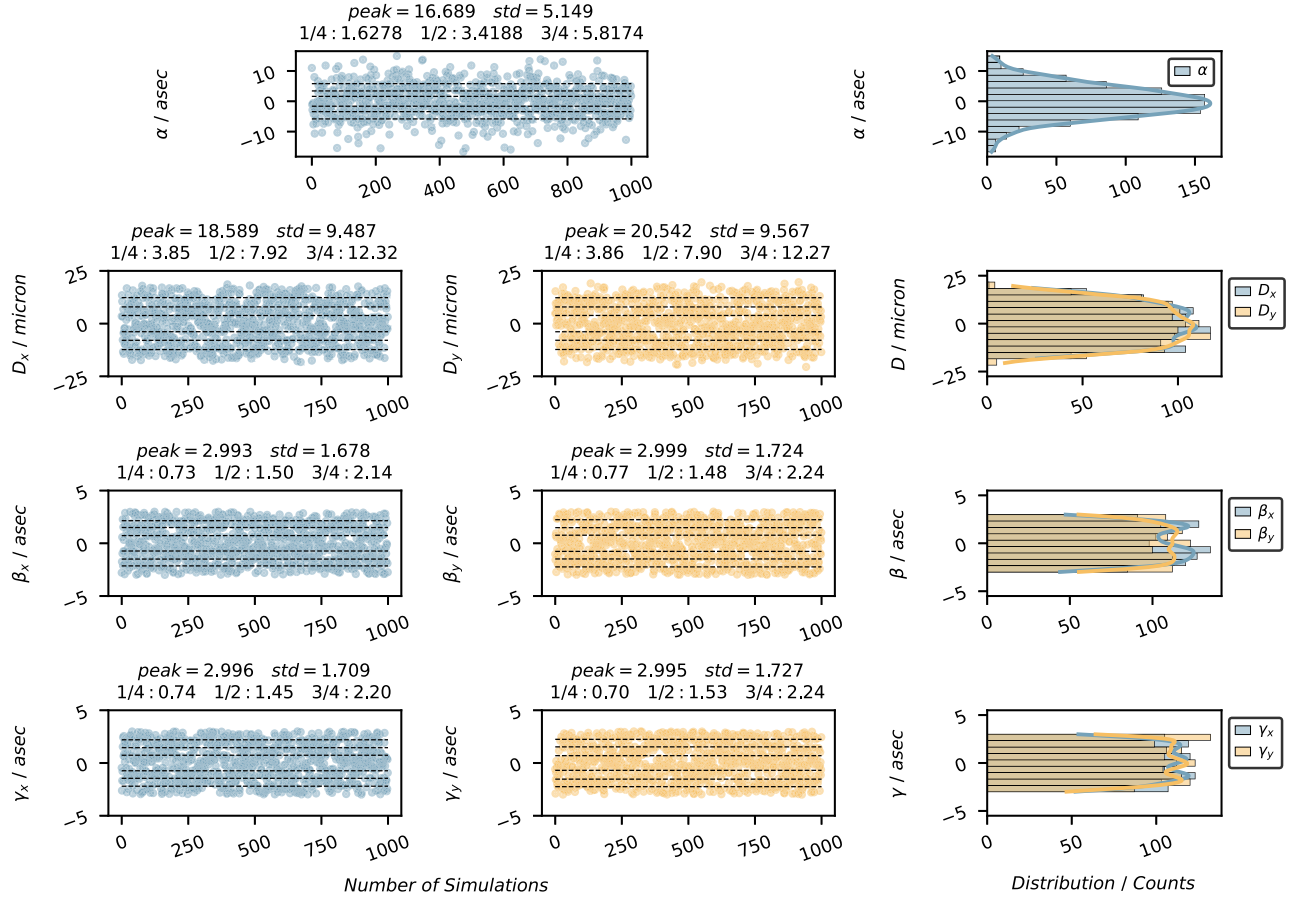
Figure 18. Inversion error distribution with the Tikhonov method upon small preset deformation.

Table 3
Inversion Error with Small Preset Deformations

	Tikhonov					Bayesian				
	1/4 Quantile	1/2 Quantile	3/4 Quantile	Peak	Std	1/4 Quantile	1/2 Quantile	3/4 Quantile	Peak	Std
α(arcsec)	1.63	3.42	5.82	16.69	5.15	1.63	3.42	5.82	16.69	5.15
$d_x(\mu m)$	3.85	7.92	12.32	18.59	9.49	2.96	6.21	10.03	24.78	8.56
$d_y(\mu m)$	3.86	7.90	12.27	20.54	9.57	2.80	6.04	10.61	23.34	8.70
β_x(arcsec)	0.73	1.50	2.14	2.99	1.68	0.52	1.02	1.66	3.86	1.39
β_y(arcsec)	0.77	1.48	2.24	3.00	1.72	0.49	1.04	1.70	4.02	1.41
γ_x(arcsec)	0.74	1.45	2.20	3.00	1.71	0.48	1.04	1.67	4.07	1.44
γ_y(arcsec)	0.70	1.53	2.24	3.00	1.73	0.49	1.01	1.78	4.21	1.47

solution to a range close to 0. This may lead to the inversion error always being the same as the actual deformation, rendering the assessment of the inversion error meaningless.

In addition, numerous practical measurements were conducted using SAS throughout the HXI assembly, launching, and in-orbit operation. Before integration into the satellite, third-party measuring equipment was capable of taking on the collimator, such as the Coordinate Measuring Machine (CMM), to validate the SAS comparatively. Figure 20 exhibits the status monitoring outcomes of the HXI at 14 crucial time points (illustrate in Table 4). The relatively flat curves in the measurement results suggest that the HXI collimator is in a
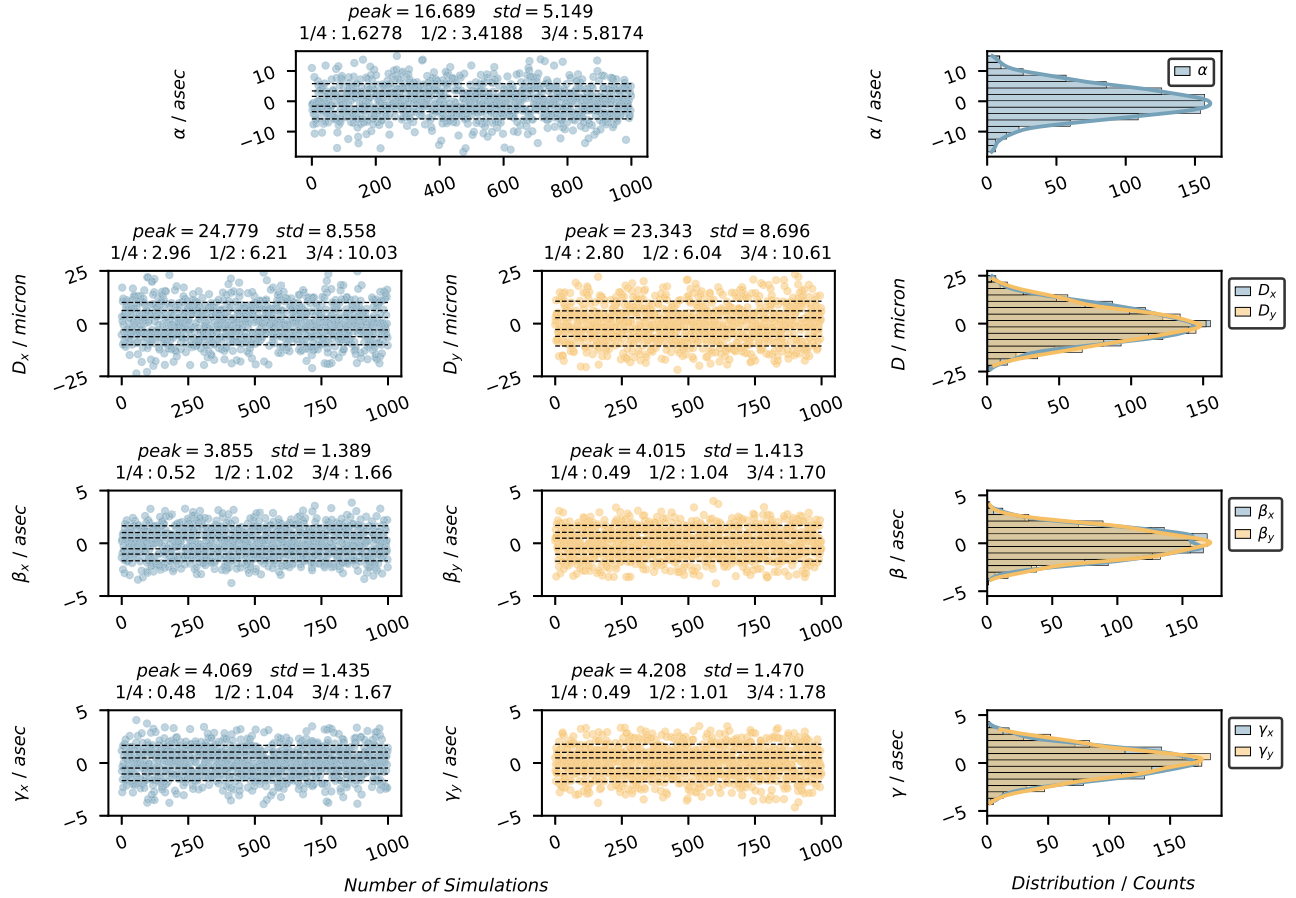
Figure 19. Inversion error distribution with the MAP method upon small preset deformation.

Table 4
Measuring Time Points

State	Time Point
1	HXI assembly completed, initial state of SAS
2	After HXI vibration test
3	After HXI thermal cycle test
4	After HXI transport test
5	Completion of all HXI tests, from then on the CMM was unavailable
6	Collimator assembled onto satellite
7	Spectrometer assembled onto satellite
8	Whole satellite assembly completed
9	After satellite environmental test
10	Before satellite launching
11	Inflight measurement
12	Inflight measurement
13	Inflight measurement
14	Inflight measurement

stable state. The SAS solution deviates from the CMM measurements, with α less than $5''$, D_x less than $10\,\mu$m, and D_y less than $13\,\mu$m. Moreover, the two regularization methods in SAS present some deviations in results, with an incoherence

less than $6\,\mu$m in D_x, and less than $5\,\mu$m in D_y, thereby demonstrating the effective usability of the SAS.

4.3. Discussion

The Tikhonov regularization and MAP methods differ in principle, however their solution results are similar and there must be a close connection between them (Antoni et al. 2023). Equation (24) shows that the penalty term present in the solution equation is of the form $\|y\|_2^2$, which is usually effective but not the only choice. By considering the general form, where the penalty term takes the form $\|Ly\|_2^2$ (Hansen 1989), the Tikhonov regularization can be expressed as

$$\arg\min_{y\in\mathbb{R}^n}\left\{\|Bx-g\|^2+\lambda^2\|Ly\|^2\right\} \tag{48}$$

where L is a discrete approximation of some operation operator on the variable y in the first kind of Fredholm integral equations (Hansen 1989, 2010), describing the interrelationships among the variables to be solved. The
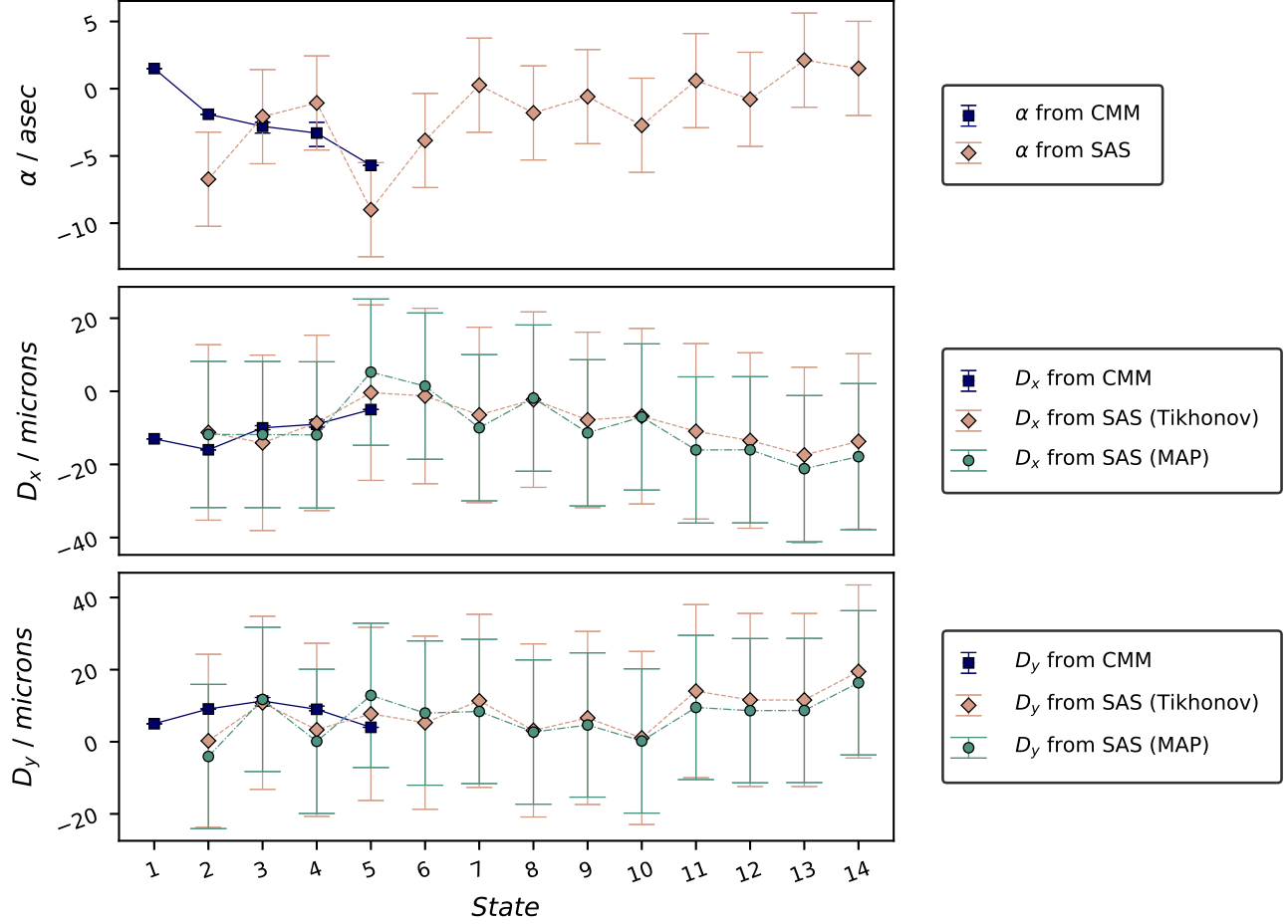
Figure 20. Practical use of SAS and CMM in significant time points. The error bars for both the Tikhonov and MAP methods are calculated as $1/2$-quantile of the error distribution with the preset deformation of $\alpha = \pm 10''$, $D = \pm 18\ \mu$m, $\beta = \pm 10''$, and $\gamma = \pm 10''$. Within these 14 measurement points, the initial five points occurred before the HXI integration into the satellite platform. This enabled the use of CMM as a comparative measurement. After state 5, HXI can no longer make use of third-party measuring devices for assistance, relying solely on the SAS measurement results.

Tikhonov regularization is a particular case where $L = I$. Upon examination of Equation (45), it is evident that in the first term, the residual norm is modified with the observation noise matrix S, while the second term outlines the covariance matrix W to depict the correlation between the observed variables y. Subsequently, if $W^{-1} = L^T L$, the form coheres with Equation (48). The form of L is related to the definition of the a priori probability, e.g., the Markov Random Field used in heat conduction problems (Jin & Zou 2008b) defines a priori probability of

$$L = \begin{bmatrix} -1 & 1 & & \\ & -1 & 1 & \\ & & \ddots & \ddots \\ & & & -1 & 1 \end{bmatrix},$$

or similar to the use of a Gaussian distribution with hyperparameters in this study, with

$$L = \begin{bmatrix} \dfrac{1}{\sigma_d} & & \\ & \dfrac{1}{\sigma_\beta} & \\ & & \dfrac{1}{\sigma_\gamma} \end{bmatrix},$$

while the y components are independent. In the actual measurement, D varies mainly due to the flatness of the satellite mounting surface and the collimator deformation caused by gravity unloading after launch. Therefore, it is set according to the standard deviation of $\sigma_d = 18\ \mu$m. The variation of β is primarily due to possible temperature changes

in the satellite mounting plane, which cause the front and rear grating substrates of the collimator to tilt. This is set according to the standard deviation of $\sigma_\beta = 10''$. The variation of γ is mainly due to changes in the observation optical axis caused by uncertainty in satellite attitude control. This is set according to the standard deviation of $\sigma_\gamma = 10''$. This implies a constraint on the range of y components in different proportions, and although this fits the prediction of the a priori probability, it does not necessarily achieve the effect of optimal regularization in terms of the form of the (48) as the larger the a priori variance makes the L smaller, which may result in an under-regularization. The assertion is indeed evident from the numerical simulation and the actual measuring results. Given the above considerations, this research employs the two regularization methods that share the common trait of being based on the regularization of generalized SVD but differ in their defining processes: the Tikhonov method builds upon the LS optimization function by incorporating solution range constraints, while the MAP method constructs the PPDF to build the optimization function through the distribution of observation noise and the solution's priori distribution. Nevertheless, their optimization functions both strive to balance the residuals and solution ranges, thus evidencing a close association between the two methods.

5. Conclusion

This paper aims at the problem that SAS is susceptible to noise from observation data during the monitoring of the HXI collimator, resulting in significant deviation of the inversion solution. Some methods are proposed to decrease the inversion error of SAS by utilizing the ARAP and regularization techniques following the physical model of SAS. The simulation data demonstrate the validity of the SAS inversion model and the efficacy of the regularization process. Additionally, the results obtained from the real test data provide evidence that these methods can realize the online monitoring function. In brief, we make some summarizations:

1. Based on the data simulation, the LS and the ARAP methods yield a measurement accuracy of about $\pm 15''$ in peak and $\pm 3''.5$ in $1/2$-quantile for the rotational deformation. The Tikhonov regularization approach results in a peak measurement error of about $D = \pm 55\,\mu m$ for the translation, and the peak measurement errors for the two optical axes are $\beta = \pm 10''$, and $\gamma = \pm 10''$, respectively. Its accuracy at the $1/2$-quantile is $D = \pm 24\,\mu m$, $\beta = \pm 5''$, and $\gamma = \pm 5''$. The measuring peak errors from the MAP method are slightly larger than those of the Tikhonov method, but the accuracy at the $1/2$-quantile is superior, that is, $D = \pm 20\,\mu m$, $\beta = \pm 3''$,

and $\gamma = \pm 3''$. All the simulated data have considered the extraction error of the light spot center;
2. The accuracy of the SAS algorithm's inversion is linked to its deformation scale. If the deformation is insignificant, the accuracy of the inversion is high, and conversely, if the deformation itself is significant, the inversion accuracy is reduced;
3. Analyzing the several times of practical test data, it has been discovered that there are disparities between the outcomes of SAS and CMM tests, specifically, α is less than $5''$, D_x is less than $10\,\mu m$, and D_y is less than $13\,\mu m$. Furthermore, disparities also exist between the Tikhonov and MAP methods, with D_x less than $6\,\mu m$ and D_y less than $5\,\mu m$.

In summary, this paper demonstrates that the regularization method significantly improves the stability of SAS's inversion calculation and enhances its robustness to observation noise pollution. Furthermore, the monitoring feature of SAS provides vital assistance in completing the HXI mission. It aids in instrument assembling and tuning during production and monitors the state throughout the entire lifecycle of HXI. Additionally, it enables the pointing of the solar orientation during in-orbit operations.

Unfortunately, there are inherent limitations in the visual measurement system, for instance, improving the light spot extraction accuracy indefinitely is not possible. Also, the solution accuracy for inversion equations is determined by optical parameters predominantly, making it difficult and inefficient to increase accuracy solely relying on data processing methods. Therefore, future research should focus on designing a more reasonable optical system to improve the robustness and anti-interference ability of inversion equations for the SAS-like monitoring systems, assisting the data stability algorithms to enhance accuracy. The study presented in this paper significantly improves the usability of SAS, allowing it to successfully perform its intended functions and make further progress toward achieving the HXI mission goals. Ultimately, we anticipate that such investigations will yield theories and techniques that can assist the design of the forthcoming flare observation instruments in the future.

ORCID iDs

Ji-Rui Yu ⓘ https://orcid.org/0000-0001-8903-2874

References

Abdulazeez, A. M., & Faizi, F. S. 2021, Turkish Journal of Computer and Mathematics Education (TURCOMAT), 12, 1563

Antoni, J., Idier, J., & Bourguignon, S. 2023, InvPr, 39, 065016

Calvetti, D., & Somersalo, E. 2018, WIREs Computational Statistics, 10, e1427

Dong, C.-Z., & Catbas, F. N. 2021, Structural Health Monitoring, 20, 692

Engl, H. W. 1987, JOTA, 52, 209

Engl, H. W., & Groetsch, C. W. 2014, Inverse and Ill-posed Problems (Amsterdam: Elsevier)

Fitzgibbon, A., Pilu, M., & Fisher, R. B. 1999, ITPAM, 21, 476

Gan, W.-Q., Yan, Y.-H., & Huang, Y. 2019a, SSPMA, 49, 059602

Gan, W.-Q., Zhu, C., Deng, Y.-Y., et al. 2019b, RAA, 19, 156

Gelman, A., Carlin, J. B., Stern, H. S., & Rubin, D. B. 1995, Bayesian Data Analysis (New York: Chapman and Hall/CRC)

Golub, G. H., & von Matt, U. 1997, J. Computational and Graphical Statistics, 6, 1

Ham, H., Wesley, J., & Hendra, H. 2019, Int. J. Electrical and Computer Eng., 9, 2394

Hansen, P. C. 1989, BIT Numerical Mathematics, 29, 491

Hansen, P. C. 1992, SIAMR, 34, 561

Hansen, P. C. 2010, Discrete Inverse Problems: Insight and Algorithms (Philadelphia, PA: SIAM)

Hashmi, A. W., Mali, H. S., Meena, A., et al. 2022, Materials Today: Proceedings, 56, 1939

Jaynes, E. T. 1968, IEEE Transactions on Systems Science and Cybernetics, 4, 227

Jiang, J.-H., Tang, H.-Z., Mohamed, M. S., Luo, S.-Y., & Chen, J.-D. 2020, ApSci, 10, 6348

Jin, B.-T., & Zou, J. 2008a, InvPr, 25, 025001

Jin, B.-T., & Zou, J. 2008b, IJNME, 76, 521

Joel, J., Fatma, G., Aseem, B., & Andreas, G. 2020, Foundations and Trends® in Computer Graphics and Vision, 12, 1

Johnston, P. R., & Gulrajani, R. M. 2000, ITBE, 47, 1293

Kabanikhin, S. I. 2008, Journal of Inverse Ill-Posed Problems, 16, 317

Krucker, S., Hurford, G. J., Grimm, O., et al. 2020, A&A, 642, A15

Mojabi, P., & LoVetri, J. 2008, Progress in Electromagnetics Research M, 1, 111

Poggio, T., Torre, V., & Koch, C. 1987, in Readings in Computer Vision, ed. M. A. Fischler & O. Firschein (San Francisco, CA: Morgan Kaufmann), 638

Sorkine, O., & Alexa, M. 2007, in Fifth Eurographics Symposium on Geometry Processing, ed. A. Belyaev & M. Garland (Goslar: Eurographics Association), 109

Su, Y., Liu, W., Li, Y.-P., et al. 2019, RAA, 19, 163

Warmuth, A., Önel, H., Mann, G., et al. 2020, SoPh, 295, 1

Zehnder, A., Bialkowski, J., Burri, F., et al. 2003, Innovative Telescopes and Instrumentation for Solar Astrophysics, 4853, 41

Zhang, Z., Chen, D.-Y., Wu, J., et al. 2019, RAA, 19, 160

Zhou, P., Wang, X.-Q., Huang, Q.-Y., & Ma, C. 2018, in 2018 2nd IEEE Advanced Information Management, Communicates, Electronic and Automation Control Conference. (IMCEC) (New Jersey: IEEE), 316

Zhuang, Y.-Z., Chen, W.-M., Jin, T., et al. 2022, Senso, 22, 3789

Zou, Z.-X., Chen, K.-Y., Shi, Z.-W., et al. 2023, Proc. IEEE, 111, 257